Meltwater lenses over the Chukchi and the Beaufort seas during summer 2019: from in-situ to synoptic view.

Alexandre Supply[1,1], Jacqueline Boutin[2,2], Nicolas Kolodziejczyk[3,3], Gilles Reverdin[4,4], Camille Lique[1,1], Jean-Luc Vergely[5,5], and Xavier Perrot[6,6]

[1]Laboratoire d'Océanographie Physique et Spatiale
[2]French National Centre for Scientific Research (CNRS)
[3]LOPS, University of Brest
[4]Sorbonne Université, CNRS/IRD/MNHN, LOCEAN-IPSL
[5]ACRI-st
[6]Ecole Normale Supérieure

November 30, 2022

Abstract

We investigate the Chukchi and the Beaufort seas, where salty and warm Pacific Water flows in from the Bering Strait and interacts with the sea ice, contributing to its summer melt. For the first time, thanks to in-situ measurements recorded by two saildrones deployed during summer 2019 and refined sea ice filtering in satellite L-Band radiometric data, we demonstrate the ability of satellite Sea Surface Salinity (SSS) observed by SMOS and SMAP to capture very fresh SSS induced by sea ice melt, referred to as meltwater lenses (MWL). The largest MWL observed by the saildrones during this period occupied a large part of the Chukchi shelf, with a SSS decrease reaching 5 pss, and persisted for up to one month. Over this MWL, measured currents and wind speed illustrate the influence of induced low SSS pattern on the air-sea momentum transfer to the upper ocean by restricting its vertical extent. Combined with satellite-based Sea Surface Temperature, satellite SSS provides a monitoring of the different water masses encountered in the region during summer 2019. Using sea ice concentration and estimated Ekman transport, we analyse the spatial variability of sea surface properties after the sea ice edge retreat over the Chukchi and the Beaufort seas. The two MWL captured by both, the saildrones and the satellite measurements, result from different dynamics. Over the Beaufort Sea, the MWL evolution follows the meridional sea ice retreat, whereas in the Chukchi Sea, a large persisting MWL is generated by advection of a sea ice filament.

Meltwater lenses over the Chukchi and the Beaufort seas during summer 2019: from in-situ to synoptic view.

Alexandre Supply[1,2], Jacqueline Boutin[3], Nicolas Kolodziejczyk[1], Gilles Reverdin[3], Camille Lique[1], Jean-Luc Vergely[4] and Xavier Perrot[5].

1 Univ. Brest, CNRS, IRD, Ifremer, Laboratoire d'Océanographie Physique et Spatiale (LOPS), IUEM, Brest 29280, France

2 CNES, Paris, France

3 Sorbonne University, LOCEAN Laboratory - IPSL, CNRS–IRD–MNHM, Paris, France

4 ACRI-ST, Guyancourt, France

5 LMD / IPSL, CNRS, ENS, PSL, Paris, France

Key points

(1) Saildrones and L-Band radiometers detect sea ice induced large SSS variability over the Chukchi and the Beaufort Sea.

(2) Low SSS patterns formed by sea ice melting influence the vertical extent of momentum transfer induced by wind stress.

(3) L-Band radiometers are able to monitor meltwater lenses with a persistence time up to more than one month reaching 5 pss SSS decrease.

Abstract

We investigate the Chukchi and the Beaufort seas, where salty and warm Pacific Water flows in from the Bering Strait and interacts with the sea ice, contributing to its summer melt. For the first time, thanks to in-situ measurements recorded by two saildrones deployed during summer 2019 and refined sea ice filtering in satellite L-Band radiometric data, we demonstrate the ability of satellite Sea Surface Salinity (SSS) observed by SMOS and SMAP to capture very fresh SSS induced by sea ice melt, referred to as meltwater lenses (MWL).

The largest MWL observed by the saildrones during this period occupied a large part of the Chukchi shelf, with a SSS decrease reaching 5 pss, and persisted for up to one month. Over this MWL, measured currents and wind speed illustrate the influence of induced low SSS pattern on the air-sea momentum transfer to the upper ocean by restricting its vertical extent.

Combined with satellite-based Sea Surface Temperature, satellite SSS provides a monitoring of the different water masses encountered in the region during summer 2019. Using sea ice concentration and estimated Ekman transport, we analyse the spatial variability of sea surface properties after the sea ice edge retreat over the Chukchi and the Beaufort seas. The two MWL captured by both, the saildrones and the satellite measurements, result from different dynamics. Over the Beaufort Sea, the MWL evolution follows the meridional sea ice retreat, whereas in the Chukchi Sea, a large persisting MWL is generated by advection of a sea ice filament.

Plain language summary

The Arctic Ocean is an area of large variations in salinity, resulting from river discharges and sea ice melt. Salinity is a main driver of ocean circulation as it determines (with seawater temperature) the seawater density. However, very little is known about salinity variations there, due to the paucity of in situ measurements near ice and in river plumes. Here, we show that novel satellite sea surface salinity captures the evolution of meltwater lenses that were identified in-situ by autonomous vehicles.

Over the Chukchi and the Beaufort seas, the sea surface salinity exhibits large seasonal changes, partly because of the sea ice melting. In this region, Pacific Water enters into the Arctic Ocean, resulting in large gradients of salinity and temperature. During summer 2019, two autonomous vehicles, named saildrones, measured the surface salinity and temperature variability during the sea ice retreat (as well as other variables, such as current profiles). These measurements allow to monitor the ocean surface and to validate surface salinity and temperature estimates from satellites.

Comparing saildrone measurements and satellite estimates, we demonstrate for the first time the satellite's ability to detect large surface salinity decreases induced by the formation of meltwater lenses.

Keywords

Sea Surface Salinity; SMOS; SMAP; Arctic Ocean; Meltwater lenses.

1. Introduction

The Arctic Ocean salinity is largely influenced by river discharges and sea ice melting. As in any cold environment, it largely determines the seawater density. Nevertheless, in-situ measurements are very sparse near sea ice and in river plumes. Combined with in-situ measurements, novel satellite Sea Surface Salinity (SSS) has the potential to contribute to a better understanding of the evolution of the Arctic sea surface properties.

In the Arctic Ocean, Pacific Water (PW) is one of the primary low salinity sources. It enters through the Bering Strait to the Chukchi Sea. Over the Chukchi Shelf, two distinct Pacific-originated water masses are commonly observed: the relatively salty Bering Sea Water (BSW; between 32 and 33 pss) and the relatively fresh Alaskan Coastal Water (ACW; between 31 and 32 pss; Coachman et al., 1975; Steele et al, 2004). ACW is mainly composed of Riverine Water (RW), with a strong contribution from the Yukon River. ACW and the easternmost branch of BSW are injected into the north of the Beaufort Gyre, while the westernmost branch is advected northward and carries PW toward the Transpolar Drift (Timmermans et al., 2014).

Woodgate and Peralta-Ferriz (2021) report on an increase of the PW transport into the Chukchi Sea since 1990, associated with an increase of the heat inflow. This trend is a part of the “borealization” affecting the Arctic Ocean (Polyakov et al., 2020). These changes have significant consequences on sea ice spatial and temporal variability (Danielson et al., 2020).

As PW brings heat to the Arctic during spring and summer, it contributes to the seasonal sea ice melt. This source of warm water may take the form of a jet penetrating in the Arctic Ocean up to the Beaufort Sea, passing by the Barrow Canyon (MacKinnon et al., 2021). During the sea ice melt and retreat, the large amount of freshwater added to sea surface may induce a strong decrease in SSS following the sea ice edge retreat during the summer. This freshening may be correlated with the distance from the sea ice edge, as described in the Beaufort Sea by Dewey et al (2017). These lenses strongly modify surface density and thus influence ocean dynamics. Induced strong stratification also influences ocean-sea-ice-atmosphere exchanges, inhibiting vertical mixing. The stratification also impacts the Near Surface Temperature Maximum (NSTM) ability to store summer heat during winter and then to influence sea ice melting the following summer (Steele et al., 2011).

Nevertheless, due to their sporadic nature and the difficulty inherent to the sea surface monitoring over the Arctic Ocean, these freshening events remain poorly documented. In this context, autonomous vehicles provide valuable information. In summer 2019, saildrones were deployed for the first time in the vicinity of sea ice in the Chukchi and Beaufort seas (Vazquez-Cuervo et al., 2021). Saildrones provide key measurements of salinity and temperature close to the ocean surface (at approximately 0.5 m depth). Their ability to measure wind speed (WS) and ocean currents is key to study how the surface freshening induced by sea ice melt evolves. However, satellite estimates, while less accurate than in-situ measurements provided by saildrones, offer a unique synoptic view.

The objective of this study is to use the synergy between satellite and in-situ measurement to document the ice melt induced freshening over the Chukchi and the Beaufort seas.

The Soil Moisture and Ocean Salinity (SMOS; 2010-present, Kerr et al., 2010, Font et al., 2010) and the Soil Moisture Active and Passive (SMAP; 2015-present, Piepmeier et al., 2017) satellites both monitor SSS at a resolution close to 43 km with a repetitivity close to 1 day at very high latitude (Vinogradova et al., 2019; Reul et al., 2020). The low Sea Surface Temperature (SST) characteristic of the Arctic Ocean results in a poor sensitivity of L-Band radiometric measurements to SSS (Meissner et al., 2016). Despite this poor sensitivity, that is somewhat compensated by the very large SSS contrasts in the Arctic (with SSS close to 35 pss for the Atlantic water and close to 0 pss for river plumes; Carmack et al., 2016), satellite SSS data have been used to characterize surface water masses in the Arctic Ocean (Olmedo et al., 2018; Tang et al., 2018). With the use of complementary variables as SST, or Colored Dissolved Organic Matter (CDOM), provided by satellites such as the Advanced Microwave Scanning Radiometer (AMSR)-2, SSS may also allow for the monitoring of Arctic river plumes sea surface variability at intra-seasonal scales (Matsuoka et al., 2016; Tarasenko et al., 2021). The long SMOS time series enables investigating inter-annual variability (Supply et al., 2020a). Nevertheless, numerous challenges remain regarding satellite derived SSS estimates in the Arctic Ocean. Due to sparse in-situ measurements, corrections using in-situ derived information and an optimal interpolation method, remains difficult (Kolodziejczyk et al., 2021). An additional limitation comes from the sea ice heterogeneity and instrument resolution, limiting the measurements closer than ~43 km from the ice edge, with difficulties in detecting and filtering small ice-covered regions. Furthermore, sea ice presence in a satellite pixel has the potential to significantly contaminate the retrieved satellite SSS: considering a brightness temperature of sea ice twice the one of sea water, a coverage of 0.2% of the surface of the considered pixel by sea ice would lead to a SSS underestimate of ~1pss. Hence, a first important step in our paper is to assess the ability of L-Band radiometers to monitor from space freshening induced by sea ice melt forming Meltwater Lenses (MWL), by comparing SMOS and SMAP SSS with the measurements from two saildrones in the vicinity of sea ice.

Vazquez-Cuervo et al. (2021) demonstrated the good agreement between SMAP SSS and saildrones SSS, with a particularly good monitoring of the Yukon River plume during summer 2019. Here, measurements carried out from the same saildrone campaign close to the sea ice are used to assess the ability of both SMOS and SMAP satellite data to monitor the SSS decrease induced by sea ice melt over the Chukchi and the Beaufort Sea (Section 3). We then discuss the largest MWL crossed by the saildrones, considering saildrones SSS and SST, as well as WS and currents measurements (Section 4). Finally, we present the evolution of sea surface properties in the Chukchi and the Beaufort seas using satellite measurements in Section 5. We discuss the results and conclude in Section 6.

2. Data and methods

The present study is limited to a period from June to September. Thus, in the following, day number corresponds to the number of days since June 1, 2019, date of this study scope beginning.

a. In-situ measurements from saildrones

i. SSS and SST

Saildrones are wind-powered oceanographic autonomous devices travelling over long distances (Mordy et al., 2017). During summer 2019, two Saildrones (Saildrones 1036 and 1037, hereafter S1036 and S1037) were deployed in the Arctic Ocean as part of the National Oceanographic Partnership Program (NOPP) – Multi Sensor Improved SST (MISST) project. Saildrones are equipped with two Conductivity-Temperature-Depth (CTD) sensors: a SBE37 sensor at 60-cm depth and a RBR sensor at 53-cm depth. Each sensor measures salinity averaged over a minute (with 12-second duration measurements sampled at 1Hz). A systematic bias of 0.17 pss is recorded between the salinities measured by the SBE37 and the RBR. Due to an unexplained large decrease in salinity on the SBE37 sensor, we choose to use the RBR salinity for comparisons with satellite SSS estimates, similarly to Vazquez-Cuervo et al. (2021).

ii. Currents

Additionally to salinity and temperature measurements, we also use current estimates from both saildrones 300kHz Teledyne Workhorse Monitor WHM300 Acoustic Doppler Current Profiler (ADCP).

The temporal resolution of the current estimates is 5 minutes with the shallowest level at 4.2m and the deepest at 102.2m and with a 2-m vertical resolution. From the currents measured at different depths, it is possible to derive the vertical shear between surface and deeper currents as:

$$Shear = \sqrt{(\frac{\partial u}{\partial z})^2 + (\frac{\partial v}{\partial z})^2}$$

With u and v zonal and meridional components of ocean velocity.

iii. WS

To study wind effect on ocean surface and to derive estimates of Ekman transport, we also use WS measurements derived from a Gill Anemometer mounted at the top of the saildrone mast, at 5 m height.

b. Satellite measurements

i. SSS

We use SSS weekly fields derived from SMOS and SMAP measurements. We build weekly SMOS SSS fields from level 2 data as described below, and use weekly SMAP SSS fields provided by JPL. Both products are daily oversampled. SMOS weekly SSS are derived following a methodology inspired from Supply et al. (2020a) to minimize the error associated to the sea ice presence and to affect as less as possible the SSS variability derived from the satellite measurements.

SMOS SSS comes from a modified version of the CEC-LOCEAN L3 Arctic, distributed by the Centre Aval de Traitement des Données SMOS (CATDS; Supply et al., 2020b). In this new version, the SMOS level 2 SSS are from the ESA Climate Change Initiative (CCI) v3.2 reprocessing described in Perrot et al. (2021). In comparison with level 2 SSS used in Supply et al. (2020a), SSS is computed with an updated dielectric constant parametrization (Boutin et al., 2020), the SMOS vicarious calibration, the so-called Ocean Target Transformation, is derived using Argo optimal interpolated SSS (Gaillard et al., 2016) instead of a climatology, and SST and wind speed used as priors in the SSS retrieval are taken from European Centre for Medium-Range Weather Forecasts (ECMWF) ERA5 instead of ECMWF forecasted fields. With respect to the methodology described in Supply et al. (2020a), we update the sea ice filtering derived from the difference between SMOS retrieved pseudo dielectric constant (Acard parameter) and the one expected from retrieved SSS and SST: instead of being applied only at level 3, sea ice filtering is applied both at level 2 (swath product) and at level 3 (weekly averaged product), which provides more consistent results when compared with the saildrones data.

SMOS SSS are averaged over 9 days on a 25km Equal-Area Scalable Earth (EASE) 2.0 grid adapted to polar areas. These fields have an effective spatial resolution close to 50 km, corresponding to the original resolution of SMOS SSS (no spatial interpolation is applied from level 2 to level 3). SSS is derived with a correction of SST-induced bias using Remote Sensing Systems (RSS) SST. Given the difficulty to find a reference to adjust absolute SSS values in the Arctic Ocean, this product does not contain any Land Sea Contamination (LSC) correction; nevertheless, in the averaging process, SMOS SSS is weighted by the Chi2 of the retrieval, and we expect it to be degraded on SMOS dwell lines largely contaminated by LSC.

When compared with saildrones measurements, this SMOS SSS product better compared with the BEC Arctic product v3.1 (Martinez et al, 2022): standard deviation of the difference (STDD) is increased up to 20% with BEC product (comparisons are shown on appendix a).

For SMAP, we use the Jet Propulsion Laboratory (JPL; Fore et al., 2019) version 4.3 8-day averaged SSS provided on a 0.25° regular grid, with a spatial interpolation from level 2 to level 3. In this product that uses a LSC correction, the effective spatial resolution of SSS is close to 60 km. The use of JPL SMAP SSS instead of SMAP SSS distributed by RSS is motivated by a less restrictive ice mask in the polar regions. Between June 19th and July 23rd 2019, SMAP was in safe mode and did not provide SSS estimates.

SMOS and SMAP SSS are provided with an uncertainty estimated by the SSS retrieval algorithm.

An additional filtering (mainly removing sea ice contaminated pixels) is applied considering SMOS and SMAP SSS retrieval uncertainties (see appendix b – only SSS estimates with an uncertainty lower than 0.6 pss are considered in the following). SSS estimates from both satellites are intercalibrated using saildrones measurements: mode of the distribution between each satellite SSS and saildrone SSS allows to define constant correction applied to SMOS and SMAP. 0.5 pss are added to SMOS SSS and 0.5 pss are subtracted to SMAP SSS. After the filtering, SMOS and SMAP SSS are finally combined in one product: SMOS+SMAP SSS, by averaging the values of the two satellites, without any ponderation by the uncertainty. Prior to this operation, SMAP is interpolated in the same 25 km EASE 2.0 grid than SMOS. These two latter steps ensure an equivalent weight of the two satellites in the average. Nevertheless, there is an exception: when a pixel is not covered by a measurement from one satellite (due for example to a different behaviour of the sea ice filtering), only the measurement from the other satellite is taken into account. Thus, between June 19th and July 23rd, SMOS+SMAP SSS correspond to SMOS SSS. We also derive an error estimate for this combined SSS product based on the uncertainties from SMOS and SMAP. This product is available on the SEANOE website (Supply et al, 2022).

Appendix-c illustrates comparisons between saildrones salinity and SSS retrieved with SMOS, SMAP or SMOS+SMAP combined products. SMOS SSS estimates are noisier than SMAP SSS estimates (Appendix c; see also satellite minus saildrones differences in Appendix b). Nevertheless, SMOS provides a better consistency than SMAP between satellite estimates and in-situ measurements considering salinities lower than 28 pss on one side and higher than 28 pss one the other. Mean of the difference (MoD) recorded between SMAP and saildrone is 0.32 pss above 28 pss and 0.00 pss below. Difference of MoD is lower between SMOS and saildrones: -0.15 pss above 28 pss and -0.10 pss below 28 pss. SMOS and SMAP instruments and retrieval methodologies present differences (prior information, sea ice filtering, etc.) inducing a different filtering of sea ice (some pixels are filtered with SMOS and not with SMAP, and inversely). Combining both products allows us to reduce the noise, increase the spatio-temporal coverage and retain the higher consistency of SMOS SSS.

ii. SST

We also make use of the SST product provided by RSS (http://www.remss.com/measurements/sea-surface-temperature/oisst-description/), which combines infrared and microwave data with an optimal interpolation . SST is provided at 9 km resolution, and then linearly interpolated on the EASE grid with a 25 km resolution.

iii. SIC

We use the Ocean and Sea Ice Satellite Application Facility (OSI-SAF) Sea Ice Concentration (SIC) derived from AMSR-2 measurements, provided by the Danish and the Norwegian Meteorological Institute. The AMSR-2 instrument is a dual-polarized and conically scanning microwave radiometer with eight channels from 6.93 GHz to 89.00 GHz enables retrieval of various geophysical parameters, such as rain rate, wind speed and SST. The Hybrid Dynamic (OSHD) algorithm operated for OSI SAF SIC retrieval uses 18.70, 36.50 and 89.00 GHz bands with spatial resolution 22 km x 14 km and 5 km x 3 km. Close to the sea ice edge, SIC estimates tend to be more uncertain in thin ice conditions or when floe sizes are not resolved by microwave radiometers (Liu et al., 2016). This limits the use of microwave radiometers to estimate SIC for filtering sea ice in L-band SSS retrieval, as L-band measurements are more sensitive to thin ice than measurements at higher frequencies.

c. Reanalyses

To derive Ekman transport, we use ECMWF ERA5 winds (zonal and meridional components, U_{ERA5} and V_{ERA5}) and ERA5 air density (ρ_{ERA5}) provided by Copernicus Climate Change Service (C3S, Hersbach et al., 2020).

d. Methodology

i. Collocations

Satellite and reanalysis estimates, as well as in-situ measurements are collocated within a one-day temporal radius (considering the central day for the satellite weekly products). All in-situ measurements present in a satellite/reanalysis pixel are averaged to correspond to one satellite (or reanalysis) estimate, which results in a non-regular temporal time step for time series, depending on the saildrone trajectory and product grid. After collocation, in-situ, reanalysis and satellite time series are linearly interpolated onto a regular temporal grid with a one-hour time step to investigate the consistency between the different sources of observations.

ii. Ekman transport

Sea surface density is derived from satellite SSS and SST. Using wind and air density from ERA5, wind stress (τ) is estimated as:

$$\tau_u = C_D . |U_{ERA5}| . U_{ERA5} . \rho_{ERA5}$$

$$\tau_v = C_D . |V_{ERA5}| . V_{ERA5} . \rho_{ERA5}$$

C_D the surface drag coefficient calculated following Foreman and Emeis (2010), $C_D = \frac{(0.051 . WS_{ERA5} - 0.14)^2}{WS_{ERA5}^2}$ and $WS_{ERA5} = \sqrt{U_{ERA5}^2 + V_{ERA5}^2}$. Combining wind stress and Sea Surface density we estimate the horizontal Ekman transport in ice-free regions as (Gill et al., 1982; Tarasenko et al., 2021):

$$T_{u_{ekm}} = \frac{\tau_v}{\rho . f}$$

$$T_{v_{ekm}} = -\frac{\tau_u}{\rho . f}$$

f is the Coriolis parameter.

3. Validation of satellite SSS along the saildrone trajectories

Figure 1 illustrates the saildrones trajectories through the Bering Strait, the Chukchi Sea, and the Beaufort Sea, following the sea ice retreat during summer 2019. The two saildrones start very close to each other (less than 5 km) but then take different paths in the Beaufort Sea (thus, at the end of the entire time series considered in the study, distance between two saildrones exceed 380 km). The two saildrones SSS and SST time series illustrate the very high

SSS and SST variability in this area, with SSS values between 25 pss and 32.5 pss and SST values between -1°C and 10°C, over 3 months (figure 2 and figure 3a, b, c and d).

Saildrones and satellite measurements are compared through the analysis of 6 specific dates corresponding to different situations, indicated on figure 1. In the following, “period X-Y” refer to the time span separating event X and event Y. The two first events correspond to two freshenings observed briefly by the saildrones in the vicinity of sea ice (event 1 - 2019/06/19 and event 2 - 2019/07/05). In the end of July, the focus is made on a large Chukchi Sea MWL (event 3 - 2019/07/25), corresponding to the end of MWL crossing by the saildrones. In August, the proximity of saildrones with sea ice edge in the Beaufort Sea is analysed (event 4 - 2019/08/08). Finally, different pathway of saildrones is observed between middle of August (event 5 - 2019/08/15), exit of the Beaufort Sea MWL, and early September (event 6 - 2019/09/05), when S1036 recorded high frequency variability.

In the Bering Strait, the saildrones cross relatively salty PW (figure 2a). During this period (prior to the event 1), many satellite SSS are filtered, consistently with the close presence of sea ice and the coastline near saildrones. Consequently, the satellite weekly SSS retrieval uncertainties remain high, between 0.4 and 0.7, rather consistent with the observed spread of satellite SSS with respect to saildrones SSS. The absolute difference between saildrones and SMOS+SMAP SSS is the largest observed, exceeding 2.5 pss (figure 3a and b). During the journey of the two saildrones toward the North, S1037 records a large decrease in SSS and SST, from more than 30 pss to 26 pss and from 5°C to -1°C (event 1). The signature of this event is much weaker on S1036 records and poorly captured by satellite SSS and SST measurements (figure 3a and b). SIC map indicates the presence of thin ice filament of low concentration (figure 4a). S1037 is closer to this filament and probably crosses a first MWL. After this event, during period 1-2, both SSS and SST increase promptly and reach values characteristic of PW. STDD during period 1-2 is the highest of the other periods. It reaches 0.92 pss between SMOS+SMAP SSS and S1036 ($STDD_{S1036}$) and 1.01 pss between SMOS+SMAP SSS and S1037 ($STDD_{S1037}$).

Event 2 corresponds to another short event of SSS and SST decrease (figure 3a, b, c and d) close to the sea ice edge (figure 4b). This time, both saildrones measure these decreases, although the freshening captured by S1037 (more than 2 pss) is stronger than captured by S1036 (less than 1 pss). This event is not detected by satellite SSS, while satellite SST shows a decrease, albeit with a weaker magnitude. WS (figure 3e and f) and surface currents (figure 3g and h) are very low during this event (close to 0 $m.s^{-1}$) but they follows and precedes larger

WS and surface currents (up to more than 10 $m.s^{-1}$ for WS and more 0.4 $m.s^{-1}$ for zonal component of surface current) recorded by the saildrones.

During period 2-3, SSS and SST decrease during a little less than 10 days followed by an increase for just over 10 days. Event 3 is recorded at the end of the crossing of the largest MWL observed by the saildrones (figure 3a and b). Figure 4c illustrates well the surface occupied by the MWL just crossed by the two saildrones. At the end of the period 2-3, the period of SSS and SST increase is associated with WS increase that exceeds 10 $m.s^{-1}$. The amplitude of the MWL is captured very well by satellite estimates of SSS and SST (figure 3a, b, c and d). During this period, SMOS+SMAP SSS STDD does not exceed 0.52 pss for $STDD_{S1036}$ and 0.73 pss for $STDD_{S1037}$. This MWL is described in more detail in section 4.

Once they exit the MWL, the saildrones crosse surface water with characteristics corresponding to PW (early in period 2-3). After the MWL, they enter the Beaufort Sea, where they record an inversion of surface currents (figure 3g and h), associated with the crossing of the Chukchi slope current.

Up to event 4, SST and SSS strongly decrease, before that the saildrones turn back once they reach the sea ice edge (after 70 days). The return to lower latitudes (period 4-5) is then associated with an increase of SSS and SST. This evolution is well observed by satellite SSS and SST ($STDD_{S1036}$ = 0.60 pss and $STDD_{S1037}$ = 0.54 pss). Nevertheless, close to the sea ice edge (and despite the sea ice filtering applied to the satellite product), the SMOS+SMAP product somewhat underestimates SSS up to 1.5 pss in the worst case (around day 70; figure 3a and b).

During period 5-6, both saildrones take different directions. S1036 heads straight back southward to the Chukchi Sea, while S1037 travels to the West. During that period, SST and SSS gradients are well reproduced by satellite measurements.

Finally, both saildrones are back in the Chukchi Sea at the end of period 5-6. In the eastern part, S1036 crosses PW while, further north, S1037 is in an area with relatively low SSS, presumably caused by freshwater associated with sea ice melt (figure 3b and 4f). For S1036, event 6 is one of the high frequency changes in satellite SSS and SST which are recorded consistently with S1036 and satellites.

Over the entire time series, the STDD of SMOS+SMAP SSS is 0.75 pss with the two saildrones. The large variability observed during the saildrones journey and the relatively low STDD allows a high correlation level between SMOS+SMAP SSS and S1036 (r=0.88) and or S1037 (r=0.90).

4. A large persistent meltwater lens in the Chukchi sea

Between day 43 and 60, both saildrones monitor a large MWL (figure 3a and b). This MWL is characterized by a large SSS decrease associated with a strong SST decrease (figure 5c), with low values persisting more than two weeks. Saildrones SSS and SST thereby reach 26 pss and 2°C respectively (corresponding to a decrease of 5 pss and 6°C compared to the values measured by the saildrone before the MWL crossing). Figure 5a shows the large variability in WS measured by S1036 between day 30 and day 70. Wind stress transfers a large momentum to the sea surface, generating a vertical current shear (figure 5b). The formed vertical current shear may be correlated to the WS module (figure 5e). In the general case (all SSS considered), correlation between WS module and vertical shear reach values close of 0.5 for the shallowest level and decrease with depth (figure 5e). As expected, S1036 shows an increase in vertical shear intensity when WS increases. Between days 37 and 47, and between days 57 and 70, WS is relatively low and no significant vertical shear is generated, in contrast to periods between days 30 and 37 and between days 47 and 57. For periods with a significant vertical shear, we compare each component of the shallowest S1036 current measurement to the respective components of Ekman transport derived from WS measured by the same saildrone. Figure 5d shows that the variability of the currents is coherent with Ekman transport during large wind speed events, at the beginning of the period (days 30 to 37) and at the end of the period (day 47 to 57 when zonal transport is associated with large meridional WS), demonstrating large influence of air-sea momentum transfer on the surface layer dynamic. However, there is an exception for the zonal component of current during the period from day 52 to day 62 that is dominated by the slope current between the Chukchi and the Beaufort Sea.

Moreover, between day 30 and day 70, the vertical shear shows a variable penetration of momentum associated with wind stress (figure 5b). When SSS is relatively high (more than 29 pss), wind events are associated with a vertical extent of current shear due to momentum transfer from wind stress. Correlation between WS module and vertical shear increase with depth and a maximum value between 10 and 15 meters. Correlation decreases to 0 between 20 and 25 meters (figure 5e). The penetration of the wind effect is less important when S1036 crosses the MWL and low SSS areas (under 29 pss). There, the wind-influenced layer is restrained at first to 10 meters. Correlation between WS module and vertical shear is maximum at the shallowest depth and reach values closes of 0 from 10 meters depth (figure 5e).

5. Sea surface variability following sea ice retreat over the Chukchi and the Beaufort seas.

During their journey, both saildrones cross various water masses. Figure 6 shows their signature in T/S diagrams, comparing in-situ and satellite observations. Satellite estimates reproduce well the variability of surface water masses. Low SSS and low SST meltwater (MW) associated with sea ice melt observed in the Beaufort Sea as well as in the Chukchi Sea, relatively warm and fresh RW, salty PW are clearly distinguishable in the T/S diagrams, from both saildrones as well as satellite measurements.

As we have shown the ability of SMOS+SMAP SSS to realistically capture SSS synoptic variability and to monitor different surface water masses, we make use of these measurements to examine the spatial and temporal context leading to the appearance of MWL. To do so, we focus on two Hovmöller diagrams of SSS, SST and Ekman transport (from satellites, for SSS and SST, and ERA5 reanalysis, for WS) along the two transects represented on figure 1. The first Hovmöller diagram is representative of the surface conditions in the Chukchi Sea and the second one of the Beaufort Sea.

The main signal in SSS visible in the first transect across the Chukchi Sea corresponds to the low SSS signal associated with the MWL visible between 72° and 75°N and between days 40 and 70 (Figure 7a). The period covered by the Hovmöller diagram starts in early June, when the full transect is sea ice covered. As sea ice retreats during June, satellite SSS measurements reveal the presence of saline surface water along the transect, albeit close to the sea ice edge where SSS and SST variability is larger and dominated by episodic low SSS event or small MWL (figure 7a). For example, on day 22, one can see a colder and fresher sea surface close to the sea ice edge for a short period of time, that follows a period centered on day 20 characterized by the presence of salty and warm water (figure 7a and b).

At the end of June and in early July, the Ekman transport is mainly oriented eastward (figure 7c and d) and may potentially drive part of the sea ice retreat by advecting sea ice in the same direction or by bringing warm water to the sea ice edge. As sea ice retreats, a large MWL becomes visible. From day 40 onward (mid-July), the large MWL described in section 4 starts to occupy the Chukchi Sea for a period longer than a month. The contrast of the surface properties found within MWL and in the surrounding region is also accentuated by the increase in SSS north of it that occurs in August (day 61). Between the middle and the end of August, an increase in Ekman transport toward the southwest (due to an increase of WS) is associated with the disappearance of the MWL, followed afterwards by a decrease in SST (day 85).

Along the second transect in the Beaufort Sea (figure 8), the sea ice only retreats in July, allowing a satellite SSS and SST monitoring that starts later than in the Chukchi Sea.

Nevertheless, this transect presents some similarities with transect 1. In July (around day 30), one can also see low SSS close to the sea ice edge. By the middle of July, a few days after the event that brings warm water under the influence of Ekman transport in the Chukchi Sea, warm and salty water is also visible in the Beaufort Sea (albeit associated with smaller SSS/SST increase). Similarly to the Chukchi Sea, this anomalous advection is followed by a large sea ice retreat. Yet, in contrast to the Chukchi Sea, the northward retreat of sea ice results in the appearance of water mass between 73° and 75°N with relatively high SSS and low SST. In August (starting on day 61), SSS contrast across the transect is strongly enhanced, due to the decrease of SSS north of 73°N and its decrease south of 73°N.

In September (starting on day 92), the surface water masses become warm and salty south of 72°N, likely under the influence of the advection of PW from the Chukchi Sea, although the Ekman transport does not exhibit any significant increase.

6. Discussion and conclusion

During summer 2019, two saildrones were deployed in the Chukchi and the Beaufort seas, allowing for the monitoring of the large sea surface variability found in this region. They crossed persistent surface water masses as RW along the Alaskan coast, PW advected in the Chukchi Sea, and the BG in the Beaufort Sea. Additionally, they also crossed regions with short-lived low SSS areas, such as in the MWL. The different observed MWL are associated with different freshening amplitudes (from a few tenth of pss to 5 pss) and are found at different distances from the sea ice edge. Measurements from the two saildrones reveal a large variability in SSS and SST in the vicinity of MWL with SSS values between 25 pss and 32.5 pss and SST values between -1°C and 10°C.

The largest MWL captured during the campaign is observed in July and August, far away from the sea ice edge, and is associated with SSS and SST decreases that reach up to 5 pss and 6°C. Saildrone measurements of ocean currents and wind further reveal that, in the presence of low SSS associated with the MWL, the increase in vertical shear driven by an increase in WS that occurred during the same period remains trapped close to the surface (down to 10m). This is likely due to an increase in stratification in the MWL resulting from the SSS decrease. This suggests that the presence of MWL and their associated stratification of the surface water properties, have the potential to modulate the ocean response to the winds, and the air-sea momentum transfer.

To provide some broader spatial and temporal context to the local in-situ observations gathered by the saildrones, we also examine satellite observations of SSS and SST. Indeed, despite the large uncertainties associated with satellite SSS estimates over the Arctic Ocean, it has been shown to provide valuable information regarding the water masses evolution in ice free regions (Tarasenko et al., 2021).

We found that SSS retrieved from the combination of SMOS and SMAP measurements captures well the variability in SSS measured by the saildrones. Associated with RSS SST estimates, we demonstrate that the satellite products provide consistent T/S diagrams representing the different water masses found at the surface of the region considered, as well as the strong decrease in SST and SSS captured by the saildrones.

Considering the temporal evolution of properties of the surface water masses following the sea ice retreat, we found that the sea ice melt over the Chukchi Sea result in a largely spread and long lasting MWL. Over the Beaufort Sea, the satellite measurements reveal the presence of lower SSS than over the Chukchi Sea, due to the overlapping of MWL over the Beaufort Gyre (SSS below 28 pss are not unusual in the Beaufort Sea, in contrast to the values measured in the Chukchi Sea). Additionally, several MWL are captured, resulting in SSS decreases. In line with the study of Dewey et al (2017), we found that the intensity of the freshening decreases as the distance from the sea ice edge increases. We found that the MWL can be associated with two different types of dynamics: over the Beaufort Sea, MWL evolution follows the meridional sea ice retreat while in the Chukchi Sea, a large persisting MWL is generated by the advection of a sea ice filament. However, regardless of the type of MWL, regions of low SSS induced by sea ice melting occupied a significant part of the Beaufort and the Chukchi Sea during summer 2019.

Further investigations are needed to fully understand the role of mixing and advection for the temporal evolution of the freshwater lenses, their occurrence and persistence, and interactions with their environment. Nonetheless, the combined use of satellites SSS and SST associated with atmospheric reanalysis, will be key to monitor the sea surface characteristics during the melting period. The ability of L-Band radiometric SSS to detect sea ice melt effects is particularly encouraging in the changing Arctic Ocean. Additional improvements could also be done regarding the strategy used for sea ice pollution mitigation. Here we voluntarily choose to remove all measurements suspected to be influenced by sea ice to ensure a reduced uncertainty. Recent studies, however, suggest that SSS could be retrieved in pixels partially covered by sea ice (Tang et al, 2021). Nevertheless, increasing proportion of areas covered by seasonal sea ice, and thus free of ice during summer, enhances the satellite ability to monitor

Arctic surface water properties. The synergy between satellite and in-situ measurements is also fundamental to understand the full dynamics of the MWL, and in particular the influence of vertical processes for their evolution.

Overall, our study also highlights the need for improvement in SSS retrievals from future satellite missions. A mission such as the proposed SMOS-HR project (Rodrıǵuez-Fernández et al., 2019), that aims to estimate SSS with L-band interferometric radiometer measurements with a 10 km resolution, would allow for a better identification of sea ice contaminated measurements and detection of thin sea ice filaments or sea ice patches extracted by ocean currents from these filaments. An improved resolution would also allow for a retrieval of SSS closer to the sea ice edge and thus to capture more accurately MWL.

Acknowledgements

AS acknowledges the support of a CNES Postdoctoral fellowship and the support of a Sorbonne Université doctoral fellowship. This work is a contribution to the TOSCA/SMOS-Ocean project supported by CNES. SMOS SSS at level 2 have been produced in the frame of the European Space Agency Climate Change Initiative CCI+SSS project.

Open research (availability statement)

We benefited from numerous data sets made freely available that are listed here: Saildrone Arctic field campaign surface measurements for NOPP-MISST project (https://podaac-tools.jpl.nasa.gov/drive/files/allData/insitu/L2/saildrone/Arctic), JPL SMAP SSS (https://podaac-tools.jpl.nasa.gov/drive/files/SalinityDensity/smap/L3/JPL/V4.3/8day_running) provided by Physical Oceanography Distributed Active Archive Center, OSI-SAF SIC provided by Norwegian Meteorological Institute (https://thredds.met.no/thredds/osisaf/osisaf_seaiceconc.html), RSS SST provided by Remote Sensing System (https://www.remss.com/measurements/sea-surface-temperature/) and ERA5 WS and air density provided by the Copernicus Climate Change Service (https://cds.climate.copernicus.eu/cdsapp#!/dataset/reanalysis-era5-single-levels?tab=overview).

References

Boutin, J., Vergely, J. L., Dinnat, E. P., Waldteufel, P., d'Amico, F., Reul, N., ... & Thouvenin-Masson, C. (2020). Correcting sea surface temperature spurious effects in salinity retrieved from spaceborne L-band Radiometer measurements. IEEE Transactions on Geoscience and Remote Sensing. DOI: 10.1109/TGRS.2020.3030488

Carmack, E.C., et al., (2016). Freshwater and its role in the Arctic marine system: sources, disposition, storage, export, and physical and biogeochemical consequences in the Arctic and global oceans. J. Geophys. Res. Biogeosci. 121, 675–717. https://doi.org/10.1002/2015JG003140.

Coachman, L. K., Aagaard, K., & Tripp, R. B. (1975). Bering Strait: the regional physical oceanography. University of Washington Press.

S.L. Danielson, O. Ahkinga, C. Ashjian, E. Basyuk, L.W. Cooper, L. Eisner, E. Farley, K.B. Iken, J.M. Grebmeier, L. Juranek, G. Khen, S.R. Jayne, T. Kikuchi, C. Ladd, K. Lu, R.M. McCabe, G.W.K. Moore, S. Nishino, F. Ozenna, R.S. Pickart, I. Polyakov, P.J. Stabeno, R. Thoman, W.J. Williams, K. Wood, T.J. Weingartner, Manifestation and consequences of warming and altered heat fluxes over the Bering and Chukchi Sea continental shelves, Deep Sea Research Part II: Topical Studies in Oceanography, Volume 177, (2020), 104781, ISSN 0967-0645, https://doi.org/10.1016/j.dsr2.2020.104781.

Dewey, S. R., Morison, J. H., & Zhang, J. (2017). An edge-referenced surface fresh layer in the Beaufort Sea seasonal ice zone. Journal of Physical Oceanography, 47(5), 1125-1144. https://doi.org/10.1175/JPO-D-16-0158.1

ECMWF, (2016). IFS Documentation CY41R2. Part II: Data Assimilation. IFS Documentation. ECMWF.

Font, J., Camps, A., Borges, A., Martin-Neira, M., Boutin, J., Reul, N., Kerr, Y.H., Hahne, A., Mecklenburg, S., (2010). SMOS: the Challenging Sea surface salinity measurement from space. Proc. IEEE 98 (5), 649–665. https://doi.org/10.1109/jproc.2009.2033096.

Fore, A., Yueh, S., Tang, W., & Hayashi, A. (2019). SMAP Salinity and Wind Speed Data User's Guide.

Gaillard, F., Reynaud, T., Thierry, V., Kolodziejczyk, N., & Von Schuckmann, K. (2016). In situ–based reanalysis of the global ocean temperature and salinity with ISAS: Variability of the heat content and steric height. Journal of Climate, 29(4), 1305-1323. https://doi.org/10.1175/JCLI-D-15-0028.1

Hersbach, H., Bell, B., Berrisford, P., Hirahara, S., Horányi, A., Muñoz‐Sabater, J., ... & Thépaut, J. N. (2020). The ERA5 global reanalysis. Quarterly Journal of the Royal Meteorological Society, 146(730), 1999-2049. https://doi.org/10.1002/qj.3803

Kerr, Y.H., et al., (2010). The SMOS Mission: new tool for monitoring key elements of the global water cycle. Proc. IEEE 98 (5), 666–687. DOI: 10.1109/JPROC.2010.2043032

Kolodziejczyk, N., Hamon, M., Boutin, J., Vergely, J. L., Reverdin, G., Supply, A., & Reul, N. (2021). Objective Analysis of SMOS and SMAP Sea Surface Salinity to Reduce Large-Scale and Time-Dependent Biases from Low to High Latitudes. Journal of Atmospheric and Oceanic Technology, 38(3), 405-421. https://doi.org/10.1175/JTECH-D-20-0093.1

Lagerloef, G., et al., (2008). The aquarius/SAC-D mission: designed to meet the salinity remote sensing challenge. Oceanography 21 (1), 68–81.

Liu J, Scott KA, Gawish A, Fieguth P. Automatic Detection of the Ice Edge in SAR Imagery Using Curvelet Transform and Active Contour. Remote Sensing. (2016); 8(6):480. https://doi.org/10.3390/rs8060480

MacKinnon, J. A., Simmons, H. L., Hargrove, J., Thomson, J., Peacock, T., Alford, M. H., ... & Wood, K. R. (2021). A warm jet in a cold ocean. Nature communications, 12(1), 1-12. https://doi.org/10.1038/s41467-021-22505-5

Martínez, J., Gabarró, C., Turiel, A., González-Gambau, V., Umbert, M., Hoareau, N., González-Haro, C., Olmedo, E., Arias, M., Catany, R., Bertino, L., Raj, R. P., Xie, J., Sabia, R., and Fernández, D., (2022). Improved BEC SMOS Arctic Sea Surface Salinity product v3.1, Earth Syst. Sci. Data, 14, 307–323, https://doi.org/10.5194/essd-14-307-2022.

Matsuoka, A., Babin, M., Devred, E.C., (2016). A new algorithm for discriminating water sources from space: a case study for the southern Beaufort Sea using MODIS Ocean color and SMOS salinity data. Remote Sens. Environ. 184, 124–138. ISSN 0034-4257. https://doi.org/10.1016/j.rse.2016.05.006.

Meissner, T., Wentz, F.J., Scott, J., Vazquez-Cuervo, J., (2016). Sensitivity of ocean surface salinity measurements from Spaceborne L-band radiometers to Ancillary Sea surface temperature. IEEE Trans. Geosci. Remote Sens. 54 (12), 7105–7111. https://doi.org/10.1109/TGRS.2016.2596100.

Mordy, C.W., E.D. Cokelet, A. De Robertis, R. Jenkins, C.E. Kuhn, N. Lawrence- Slavas, C.L. Berchok, J.L. Crance, J.T. Sterling, J.N. Cross, P.J. Stabeno, C. Meinig, H.M. Tabisola, W. Burgess, and I. Wangen. (2017). Advances in ecosystem research: Saildrone surveys of oceanography, fish, and marine mammals in the Bering Sea. Oceanography 30(2):113–115, https://doi.org/10.5670/oceanog.2017.230.

Olmedo, E., Gabarró, C., González-Gambau, V., Martínez, J., Ballabrera-Poy, J., Turiel, A., Portabella, M., Fournier, S., Lee, T., (2018.) Seven years of SMOS Sea surface salinity at high latitudes: variability in Arctic and sub-Arctic regions. Remote Sens. 10, 1772. https://doi.org/10.3390/rs10111772.

Peralta-Ferriz, C., & Woodgate, R. A. (2017). The dominant role of the East Siberian Sea in driving the oceanic flow through the Bering Strait—Conclusions from GRACE ocean mass satellite data and in situ mooring observations between 2002 and 2016. Geophysical Research Letters, 44(22), 11-472. https://doi.org/10.1002/2017GL075179

Perrot X. et al., "CCI+SSS, A New SMOS L2 Reprocessing Reduces Errors on Sea Surface Salinity Time Series," 2021 IEEE International Geoscience and Remote Sensing Symposium IGARSS, (2021), pp. 7457-7460, doi: 10.1109/IGARSS47720.2021.9554451.

Polyakov, I. V., Alkire, M., Bluhm, B., Brown, K., Carmack, E. C., Chierici, M., ... and Wassmann, P. (2020). Borealization of the Arctic Ocean in response to anomalous advection from sub-Arctic seas. https://doi.org/10.3389/fmars.2020.00491

Piepmeier, J.R., et al., (2017). SMAP L-band microwave radiometer: instrument design and first year on orbit. IEEE Trans. Geosci. Remote Sens. 55 (4), 1954–1966. https://doi.org/10.1109/TGRS.2016.2631978.

Reul, N., Grodsky, S.A., Arias, M., Boutin, J., Catany, R., Chapron, B., D'Amico, F., Dinnat, E., Donlon, C., Fore, A., Fournier, S., Guimbard, S., Hasson, A., Kolodziejczyk, N., Lagerloef, G., Lee, T., Le Vine, D.M., Lindstrom, E., Maes, C., Mecklenburg, S., Meissner, T., Olmedo, E., Sabia, R., Tenerelli, J., Thouvenin-Masson, C., Turiel, A., Vergely, J.L., Vinogradova, N., Wentz, F., Yueh, S., (2020). Sea surface salinity estimates from spaceborne L-band radiometers: an overview of the first decade of observation (2010–2019). Remote Sens. Environ. 242, 111769. ISSN 0034–4257. https://doi.org/10.1016/j.rse.2020.111769.

Rodrıǵuez-Fernández, Anterrieu, et al., (2019). SMOS-HR: a high-resolution L-band passive radiometer for earth science and applications. IEEE Symp. Geosci. Remote Sens. 2019, 8392–8395. DOI: 10.1109/IGARSS.2019.8897815

Saildrone. (2020). Saildrone Arctic NOPP-MISST Field Campaign Products. Ver. 1.0. PO.DAAC, CA, USA. Dataset accessed [2021-10-11] at https://doi.org/10.5067/SDRON-NOPP0

Steele, M., Morison, J., Ermold, W., Rigor, I., Ortmeyer, M., & Shimada, K. (2004). Circulation of summer Pacific halocline water in the Arctic Ocean. Journal of Geophysical Research: Oceans, 109(C2). https://doi.org/10.1029/2003JC002009

Steele, M., Ermold, W., & Zhang, J. (2011). Modeling the formation and fate of the near-surface temperature maximum in the Canadian Basin of the Arctic Ocean. Journal of Geophysical Research: Oceans, 116(C11). https://doi.org/10.1029/2010JC006803

Stroeve, J., & Notz, D. (2018). Changing state of Arctic sea ice across all seasons. Environmental Research Letters, 13(10), 103001. https://doi.org/10.1088/1748-9326/aade56

Supply A., J. Boutin, J.-L. Vergely, N. Kolodziejczyk, G. Reverdin, N. Reul, A. Tarasenko, (2020a), New insights into SMOS sea surface salinity retrievals in the Arctic Ocean, Remote Sensing of Environment, Volume 249, 112027, ISSN 0034-4257, https://doi.org/10.1016/j.rse.2020.112027.

Supply A., Boutin J., Vergely J.-L., Kolodziejczyk N., Reverdin G., Reul N., Tarasenko A. (2020b). SMOS ARCTIC SSS L3 maps produced by CATDS CEC LOCEAN. SEANOE. https://doi.org/10.17882/71909

Supply A., Boutin J., Kolodziejczyk N., Reverdin G., Lique C., Vergely J.-L., Perrot X. (2022). SMOS and SMAP combined SSS L3 maps over the Chukchi and the Beaufort seas during summer 2019. SEANOE. https://doi.org/10.17882/87747

Tang, W., Yueh, S., Yang, D., Fore, A., Hayashi, A., Lee, T., Fournier, S., Holt, B., (2018). The potential and challenges of using soil moisture active passive (SMAP) sea surface salinity to monitor Arctic Ocean freshwater changes. Remote Sens. https://doi.org/ 10.3390/rs10060869.

Tang W., Yueh S., Fore A., Hayashi A., Steele M. (2021). An Empirical Algorithm for Mitigating the Sea Ice Effect in SMAP Radiometer for Sea Surface Salinity Retrieval in the Arctic Seas. IEEE Journal of Selected Topics in Applied Earth Observations and Remote Sensing. PP. 1-1. 10.1109/JSTARS.2021.3127470.

Tarasenko, A. and Supply, A. and Kusse-Tiuz, N. and Ivanov, V. and Makhotin, M. and Tournadre, J. and Chapron, B. and Boutin, J. and Kolodziejczyk, N. and Reverdin, G., (2021), Properties of surface water masses in the Laptev and the East Siberian seas in summer 2018 from in situ and satellite data, Ocean Science, 221-247, 10.5194/os-17-221-2021

Timmermans, M.-L., A. Proshutinsky, E. Golubeva, J. M. Jackson, R. Krishfield, M. McCall, G. Platov, J. Toole, W. Williams, T. Kikuchi, and S. Nishino (2014), Mechanisms of Pacific Summer Water variability in the Arctic's Central Canada Basin, J. Geophys. Res. Oceans, 119, 7523–7548, doi:10.1002/2014JC010273.

Vazquez-Cuervo, J., Gentemann, C., Tang, W., Carroll, D., Zhang, H., Menemenlis, D., ... & Steele, M. (2021). Using Saildrones to Validate Arctic Sea-Surface Salinity from the SMAP

Satellite and from Ocean Models. Remote Sensing, 13(5), 831. https://doi.org/10.3390/rs13050831

Vinogradova, N., Lee, T., Boutin, J., Drushka, K., Fournier, S., Sabia, R., Stammer, D., Bayler, E., Reul, N., Gordon, A., Melnichenko, O., Li, L., Hackert, E., Martin, M., Kolodziejczyk, N., Hasson, A., Brown, S., Misra, S., Lindstrom, E., (2019). Satellite salinity observing system: recent discoveries and the way forward. Front. Mar. Sci. 6, 243. https://doi.org/10.3389/fmars.2019.00243.

Woodgate, R. A., & Aagaard, K. (2005). Revising the Bering Strait freshwater flux into the Arctic Ocean. Geophysical Research Letters, 32(2). https://doi.org/10.1029/2004GL021747

Woodgate, R., & Peralta-Ferriz, C. (2021). Warming and Freshening of the Pacific Inflow to the Arctic From 1990-2019 Implying Dramatic Shoaling in Pacific Winter Water Ventilation of the Arctic Water Column. Geophysical Research Letters, 48(9), e2021GL092528. https://doi.org/10.1029/2021GL092528

Yin X., J. Boutin, and P. Spurgeon, "Biases Between Measured and Simulated SMOS Brightness Temperatures Over Ocean: Influence of Sun," IEEE Journal of Selected Topics in Applied Earth Observations and Remote Sensing, vol. 6, no. 3, pp. 1341-1350, (2013). DOI: 10.1109/jstars.2013.2252602

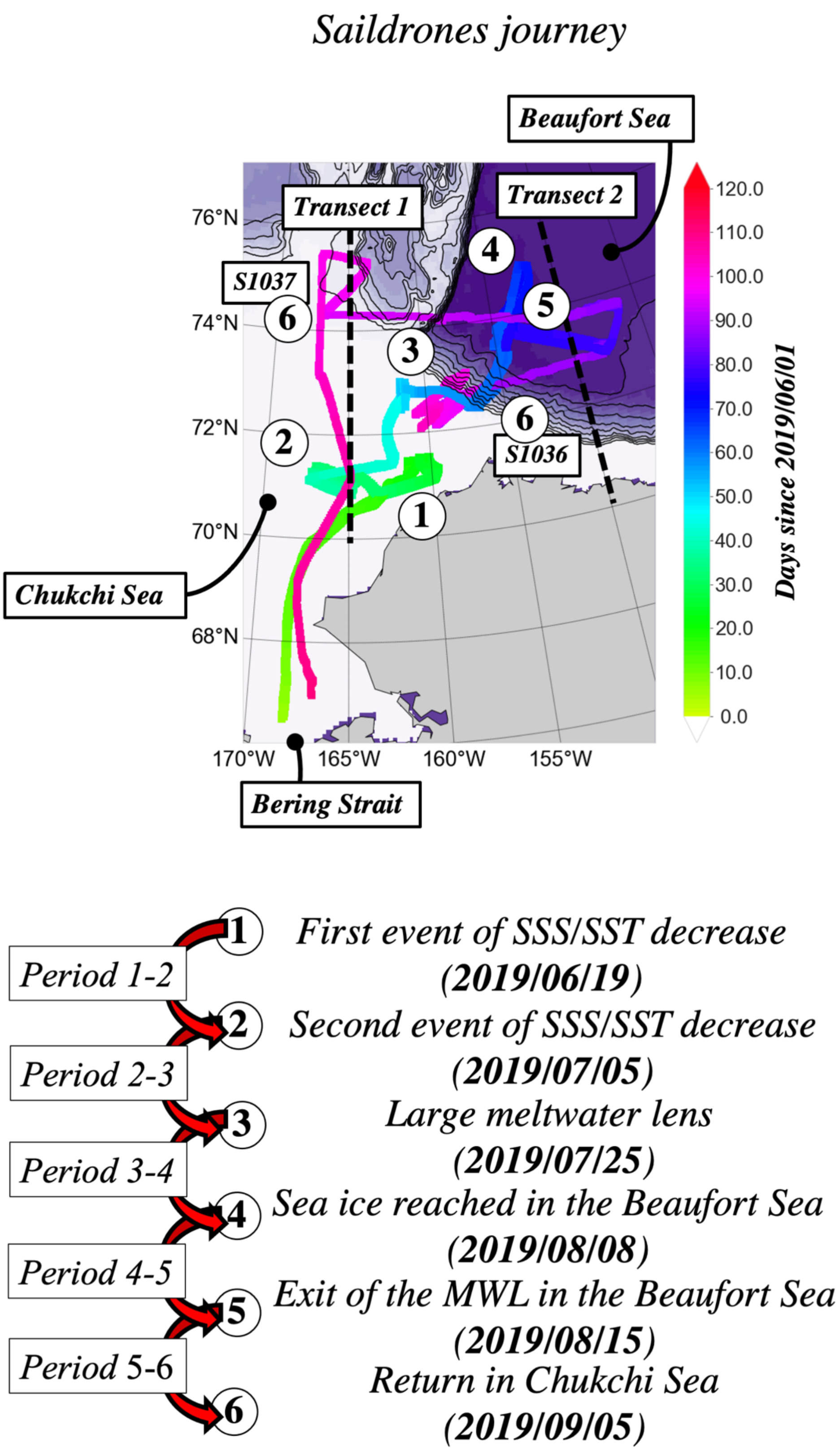

Figure 1: Saildrone trajectory (colours corresponding to the day number) overlayed on bathymetry. The numbers indicate the various stages described in the text. The positions of

the transects shown on figure 7 and figure 8 indicated with dashed lines - background colours indicate the bathymetry.

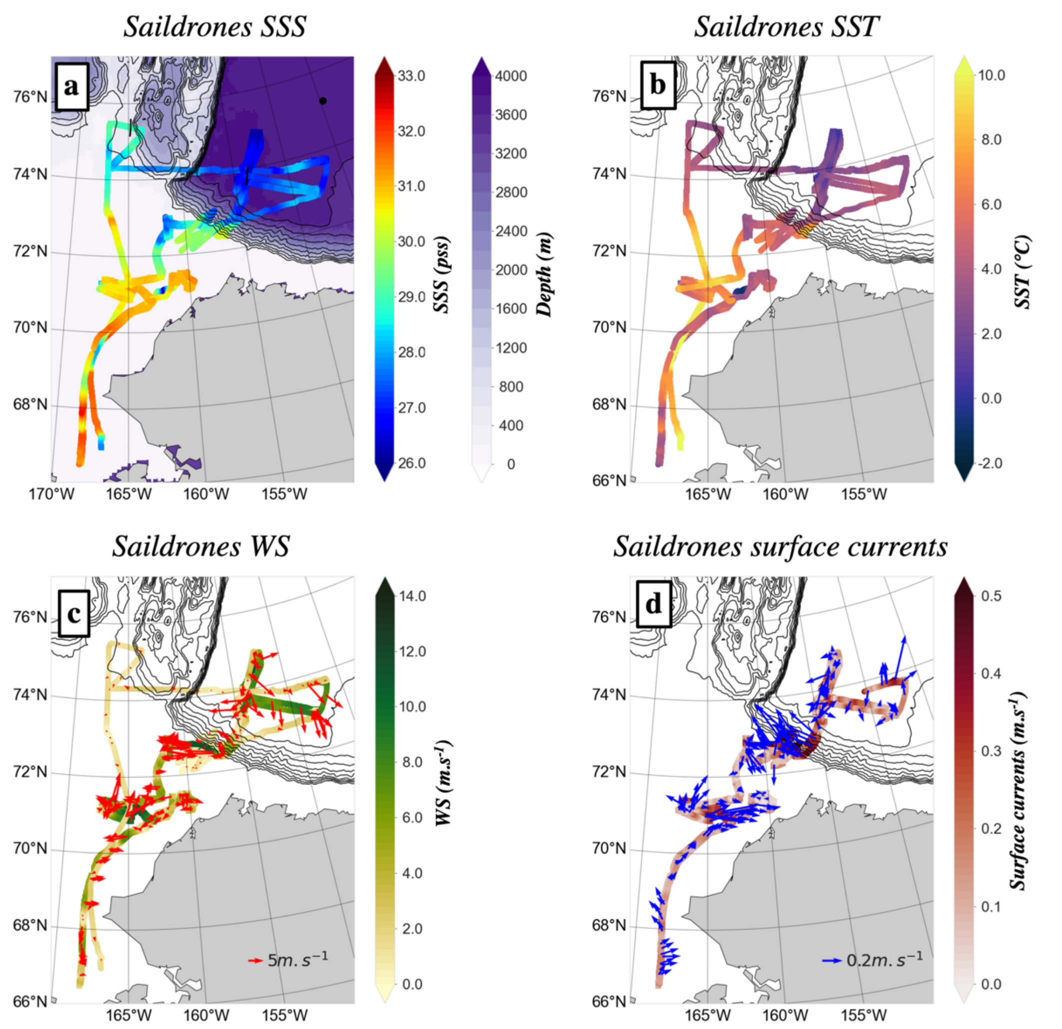

Figure 2: Saildrone a) SSS measurements (background colours indicate the bathymetry) ; b) SST measurements ; c) WS measurements (oriented arrow for direction, scaled with WS magnitude); d) surface currents measurements (oriented arrow for direction, scaled with currents magnitude) in the Bering Strait, Chukchi and Beaufort Sea from June to September 2019.

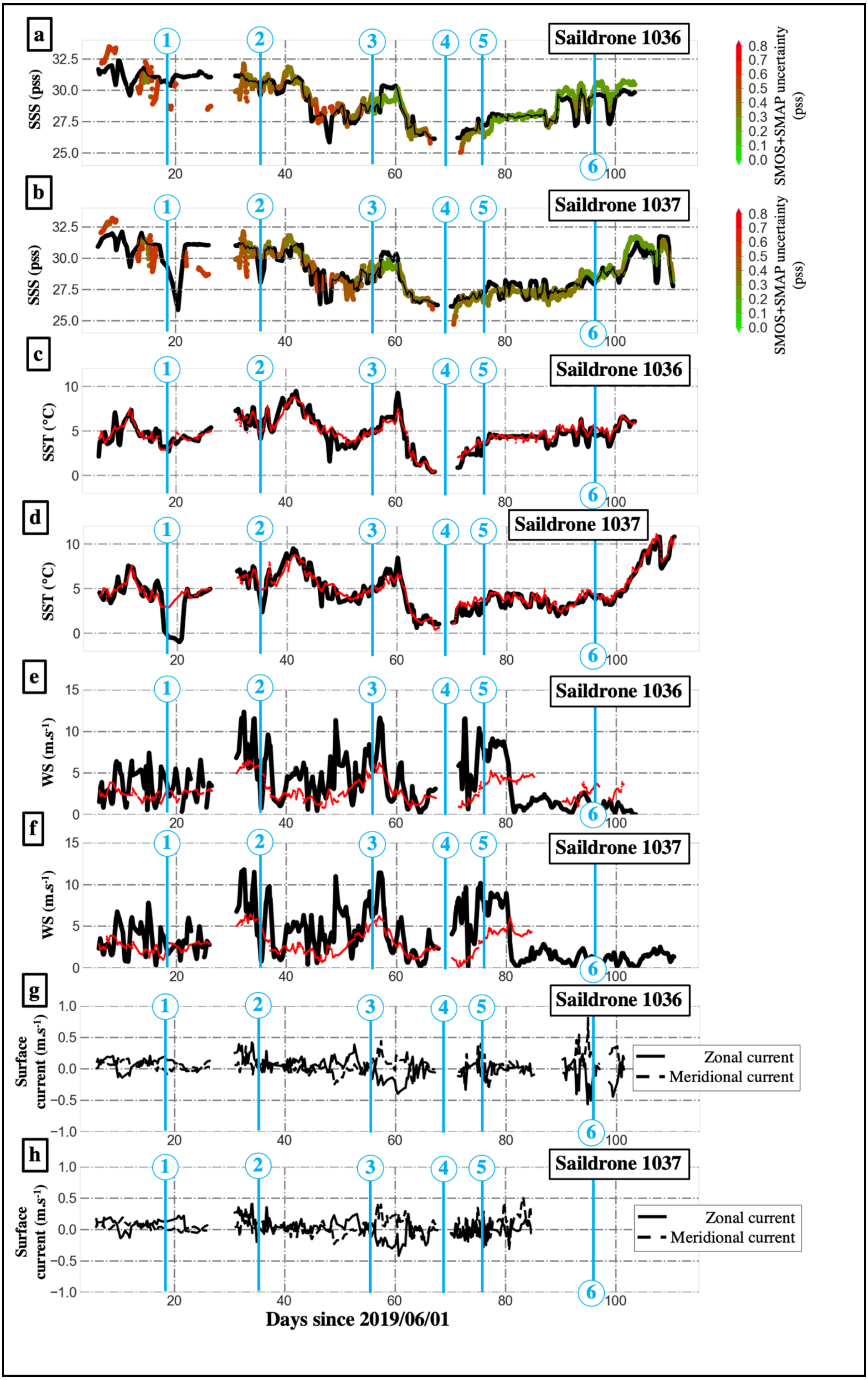
a
Saildrone 1036
SSS (pss)
SMOS+SMAP uncertainty (pss)
b
Saildrone 1037
SSS (pss)
SMOS+SMAP uncertainty (pss)
c
Saildrone 1036
SST (°C)
d
Saildrone 1037
SST (°C)
e
Saildrone 1036
WS (m.s-1)
f
Saildrone 1037
WS (m.s-1)
g
Saildrone 1036
Surface current (m.s-1)
Zonal current
Meridional current
h
Saildrone 1037
Surface current (m.s-1)
Zonal current
Meridional current
Days since 2019/06/01

Figure 3: a) S1036 SSS measurement time series (black) and SMOS+SMAP collocated SSS in colour (colour for SSS uncertainty) ; b) S1037 SSS measurement time series (black) and SMOS+SMAP collocated SSS in colour (colour for SSS uncertainty); c) S1036 SST measurement time series (black) and RSS collocated SST (red) ; d) S1037 SST measurement time series (black) and RSS collocated SST (red); e) S1036 WS measurement time series (black) and ERA5 collocated WS (red) ; f) S1037 WS measurement time series (black) and ERA5 collocated WS (red); g) S1036 surface currents measurements time series ; h) S1037 surface currents measurements time series. The blue numbers indicate the various stages described in the text. See similar time series of SMOS and SMAP SSS considered independently in appendix d.

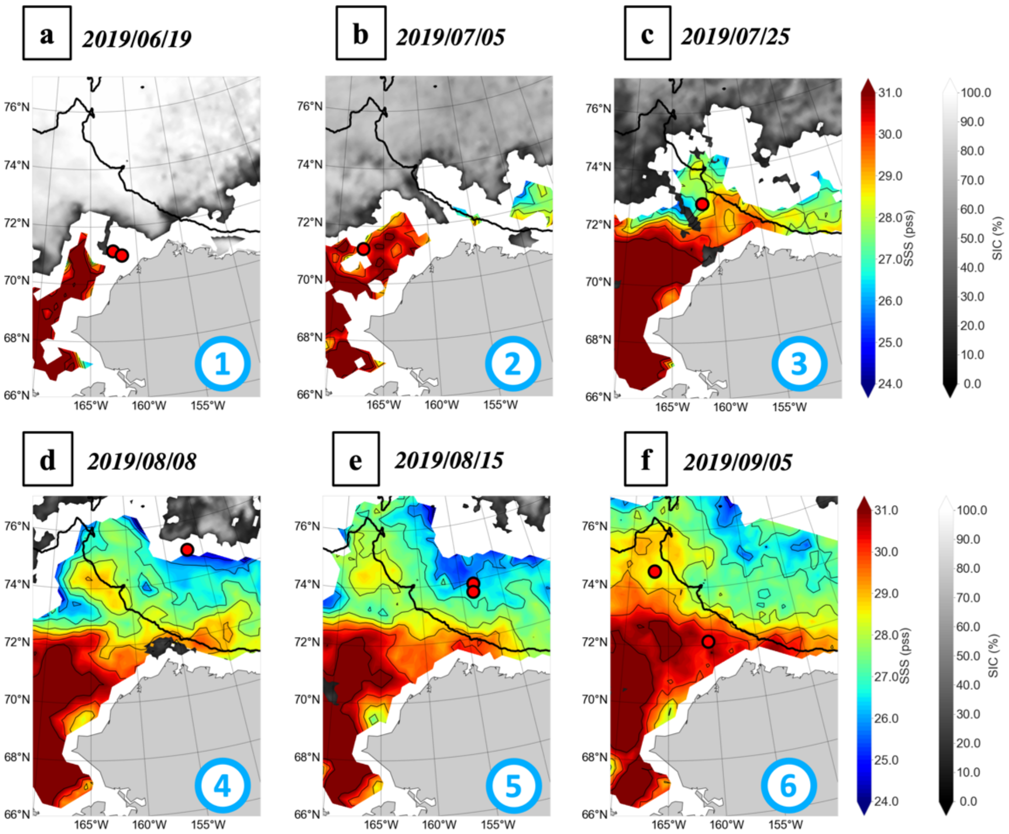

Figure 4: SMOS+SMAP SSS and OSI-SAF SIC A) for 2019/06/19 B) for 2019/07/05 C) for 2019/07/25 D) for 2019/08/08 E) for 2019/08/15 F) for 2019/09/05. Black bold line for

isobath 500m. Red dots indicate the saildrone positions on that day. See similar maps of SMOS and SMAP SSS considered independently in appendix e and f. The blue numbers indicate the various stages described in the text.

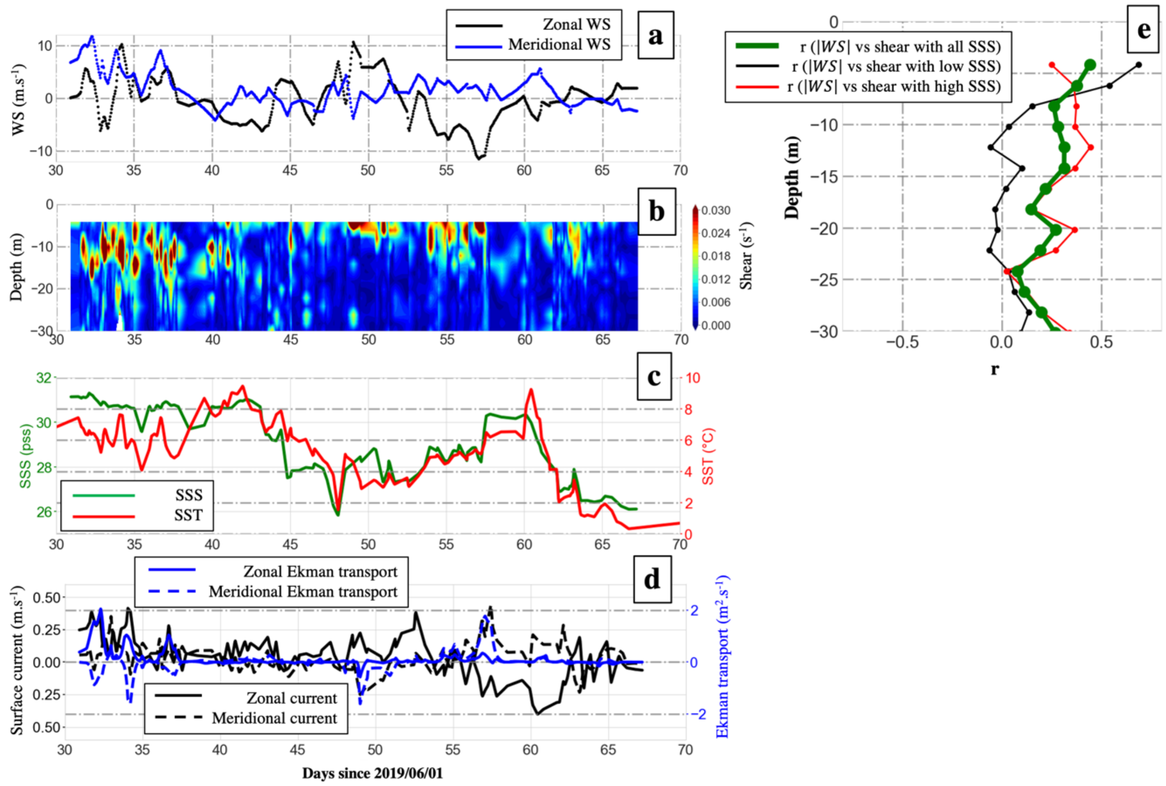

Figure 5: S1036 measurements between day 30 and 70 (since 2019/06/01) of a) zonal (black) and meridional (blue) component of WS; b) vertical shear between 0 and 30 m depth computed from currents; c) SSS (green) and SST (red); d) zonal and meridional component of surface current (black) and estimated Ekman transport (blue); e) correlation between WS module and shear as a function depth for all SSS (green), low SSS (under 29 pss, black) and high SSS (above 29 SSS, red).

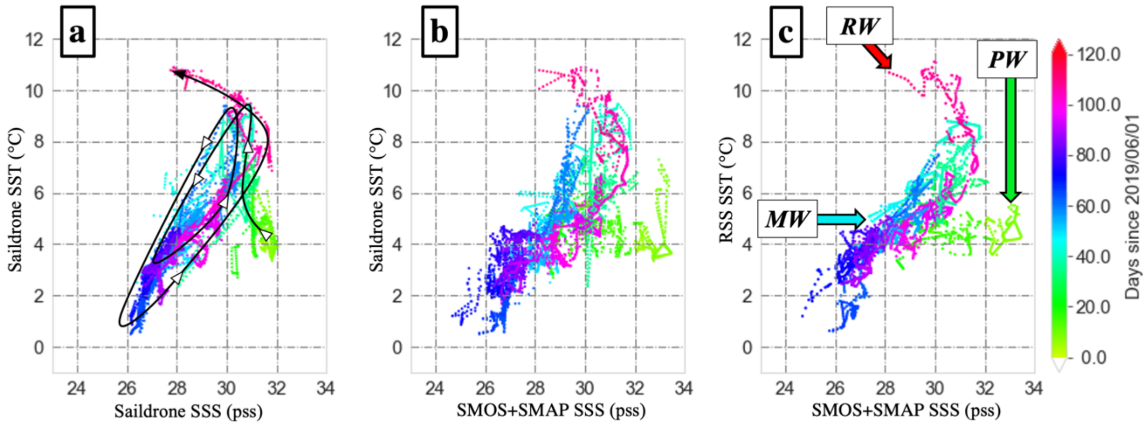

Figure 6: T/S diagrams from (a) in-situ S1037 SST and SSS, (b) in-situ S1037 SST and SMOS+SMAP SSS collocated with S1037 trajectory, and (c) RSS SST and SMOS+SMAP SSS collocated with S1037 trajectory. On (a) the arrows show the saildrone trajectory. See the text for the name of the different water masses indicated on the (c) diagram.

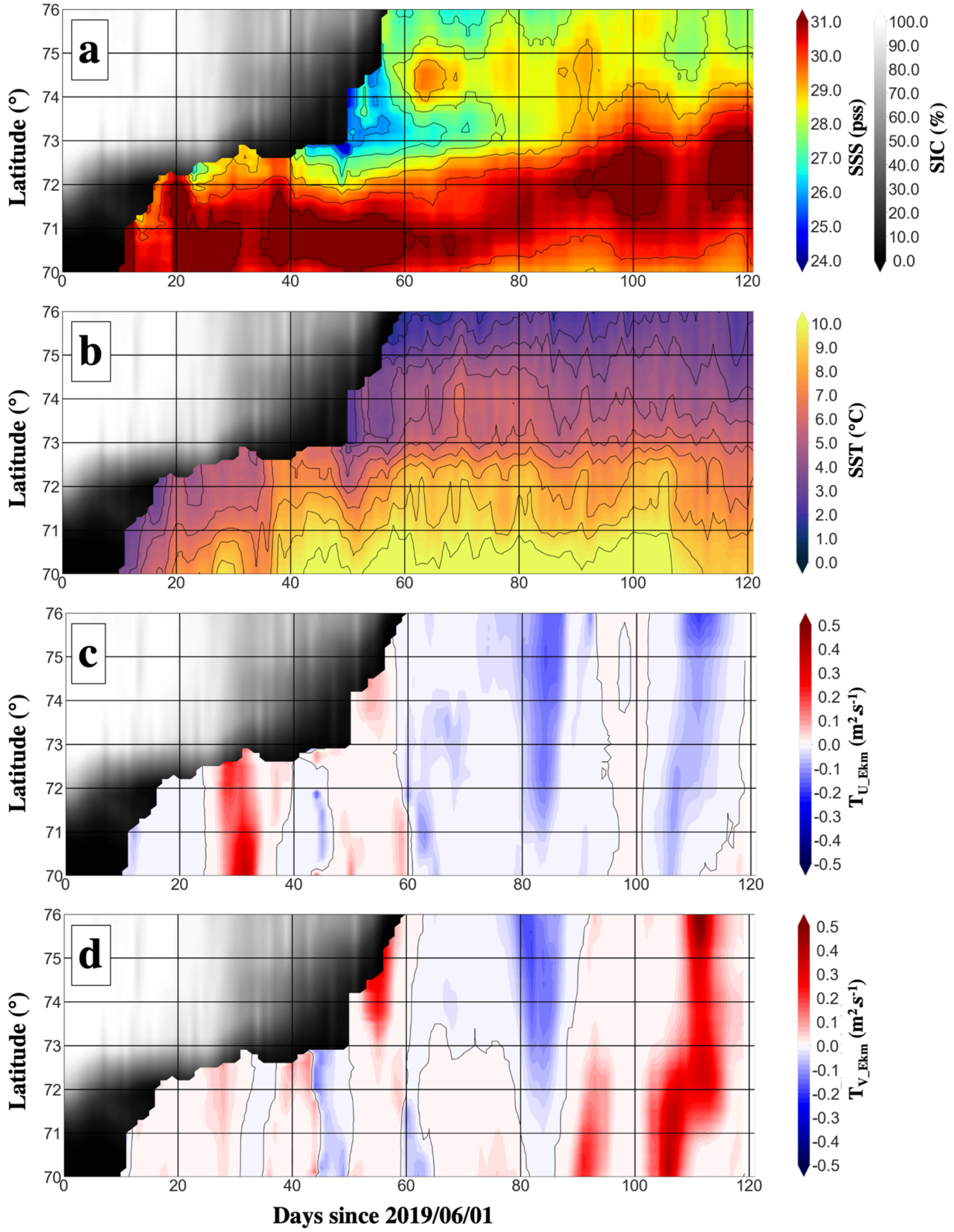

Figure 7: Hovmöller diagrams along transect 1 in the Chukchi Sea (figure 2; between 70°N and 76°N at 165°W): a) SMOS+SMAP SSS; b) RSS SST; c) zonal component of Ekman transport; d) meridional component of Ekman transport.

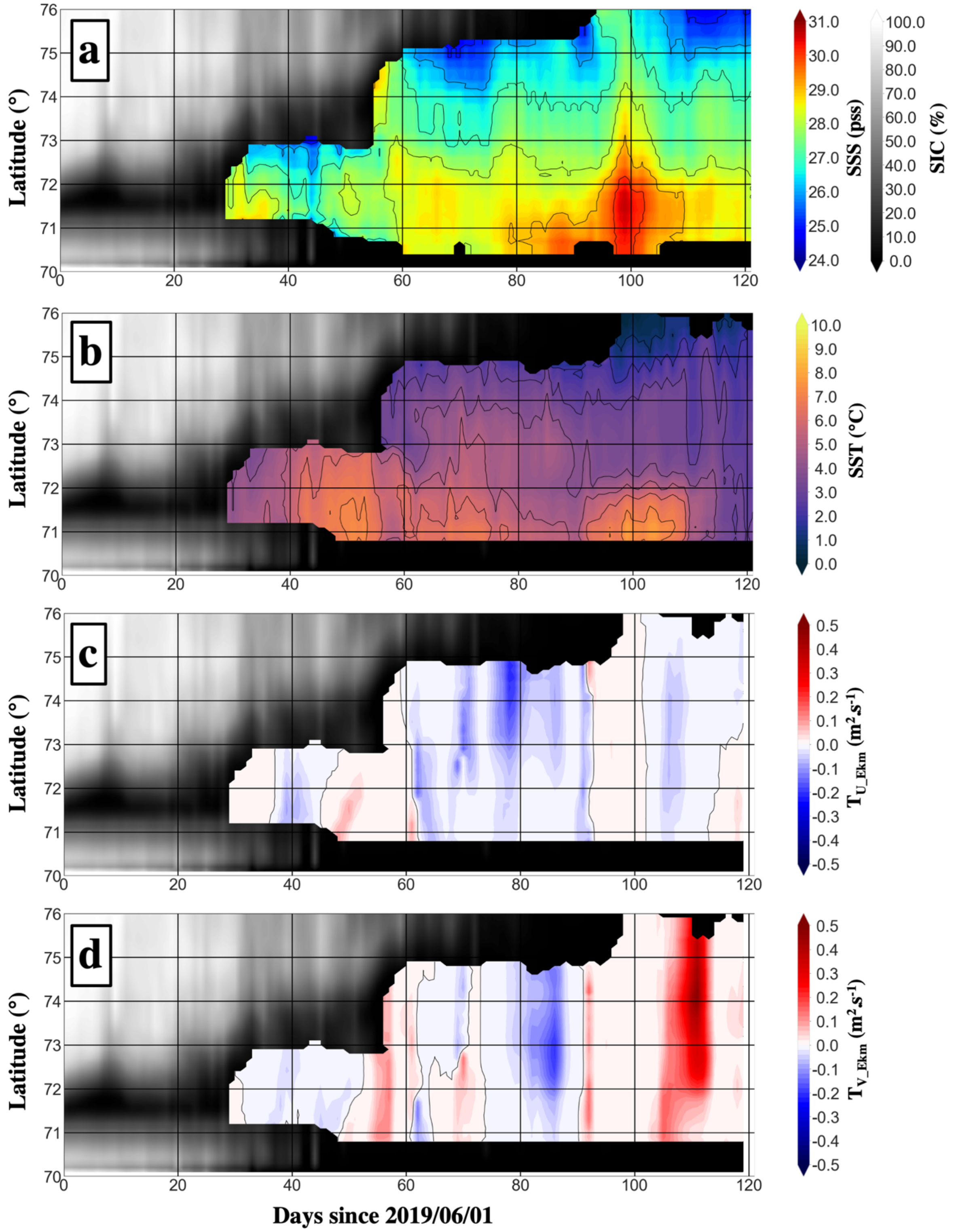

Figure 8: Hovmöller diagrams along transect 2 in the Beaufort Sea (figure 2; between 70°N and 76°N at 150°W): a) L-Band SSS; b) RSS SST; c) zonal component of Ekman transport;

d) meridional component of Ekman transport.

Supporting information

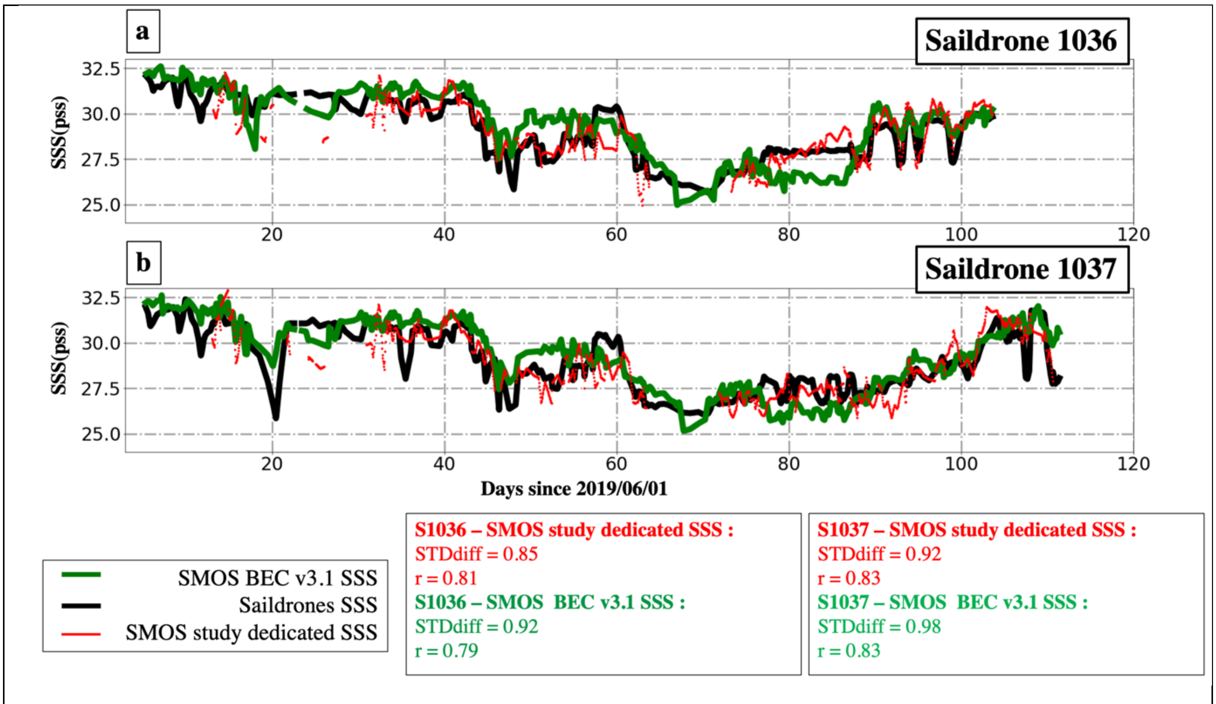

Appendix-a: a) S1036 SSS measurement time series (black), SMOS study dedicated SSS collocated SSS (red) and SMOS BEC v3.1 collocated SSS (green); b) S1037 SSS measurement time series (black), SMOS study dedicated SSS collocated SSS (red) and SMOS BEC v3.1 collocated SSS (green).

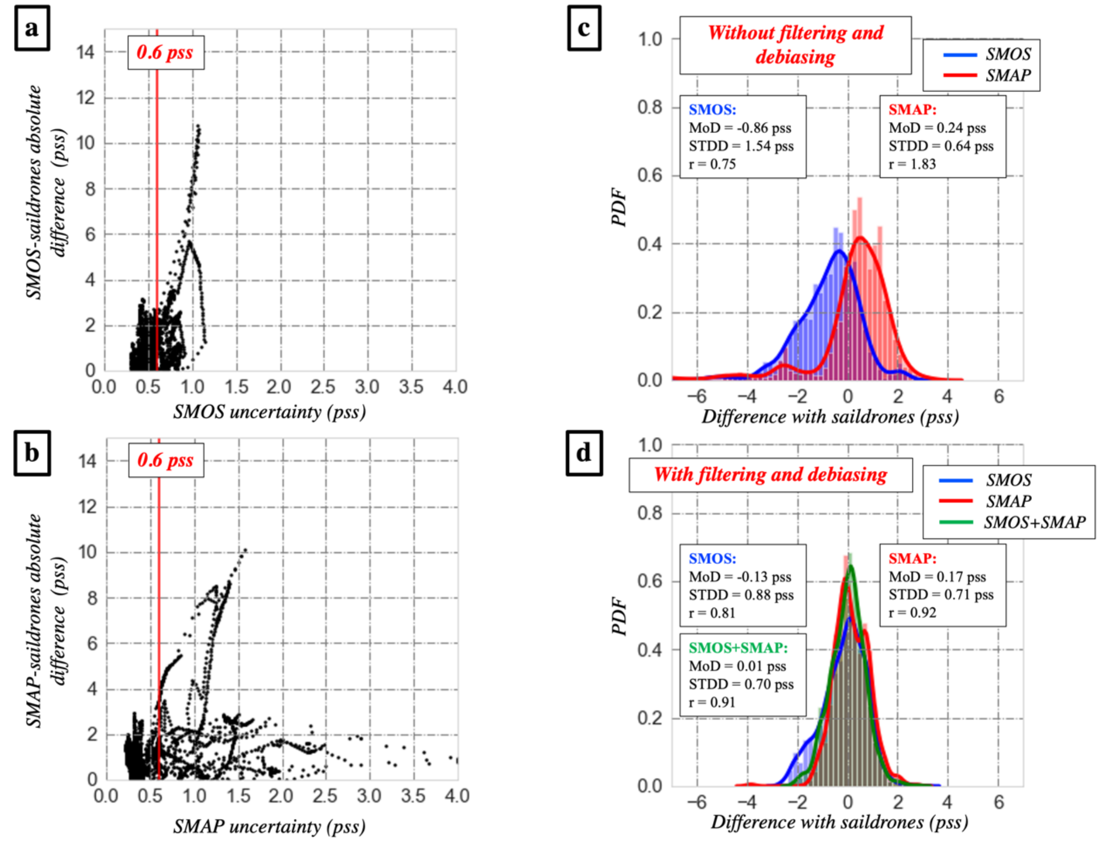

Appendix-b: a) Scatterplot of absolute difference between SMOS SSS and saildrones SSS versus SMOS SSS uncertainty (uncertainty threshold indicated in magenta); b) Scatterplot of absolute difference between SMAP SSS and saildrones SSS versus SMAP SSS uncertainty (uncertainty threshold indicated in magenta); c) Distributions of differences between SMOS and SMAP SSS, and saildrones SSS without filtering and debiasing; d) Distributions of differences between SMOS, SMAP and L-Band SSS, and saildrones SSS with filtering and debiasing.

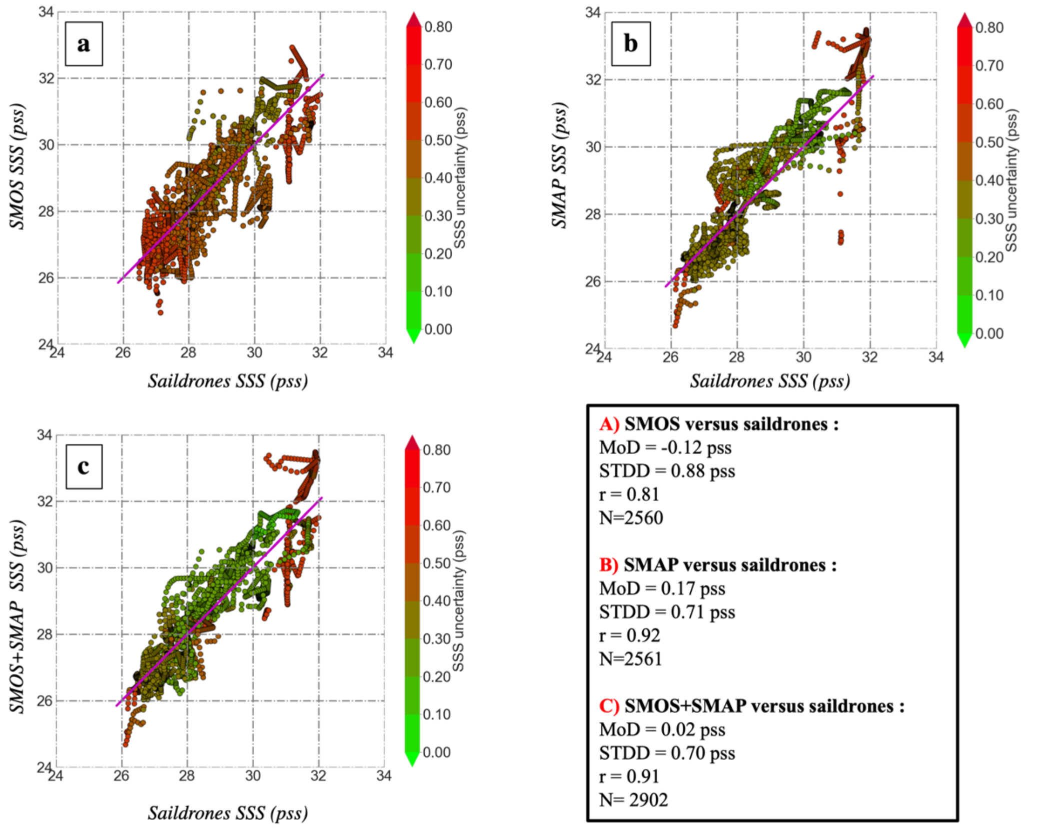
a
SMOS SSS (pss)
Saildrones SSS (pss)
SSS uncertainty (pss)
b
SMAP SSS (pss)
Saildrones SSS (pss)
SSS uncertainty (pss)
c
SMOS+SMAP SSS (pss)
Saildrones SSS (pss)
SSS uncertainty (pss)
A) SMOS versus saildrones :
MoD = -0.12 pss
STDD = 0.88 pss
r = 0.81
N=2560
B) SMAP versus saildrones :
MoD = 0.17 pss
STDD = 0.71 pss
r = 0.92
N=2561
C) SMOS+SMAP versus saildrones :
MoD = 0.02 pss
STDD = 0.70 pss
r = 0.91
N= 2902

Appendix-c: SMOS, SMAP and SMOS+SMAP SSS validation performances after debiasing and filtering. Scatterplot of SSS, with satellite SSS retrieved uncertainties in colour: a) SMOS SSS versus Saildrones SSS; b) SMAP SSS versus Saildrones SSS; c) SMOS+SMAP SSS versus Saildrones SSS. Table is for statistical indicators (MoD = Mean of Difference, STDD = STandard Deviation of Difference, r = correlation coefficient and N = Number of collocations between satellite SSS and saildrone salinity).

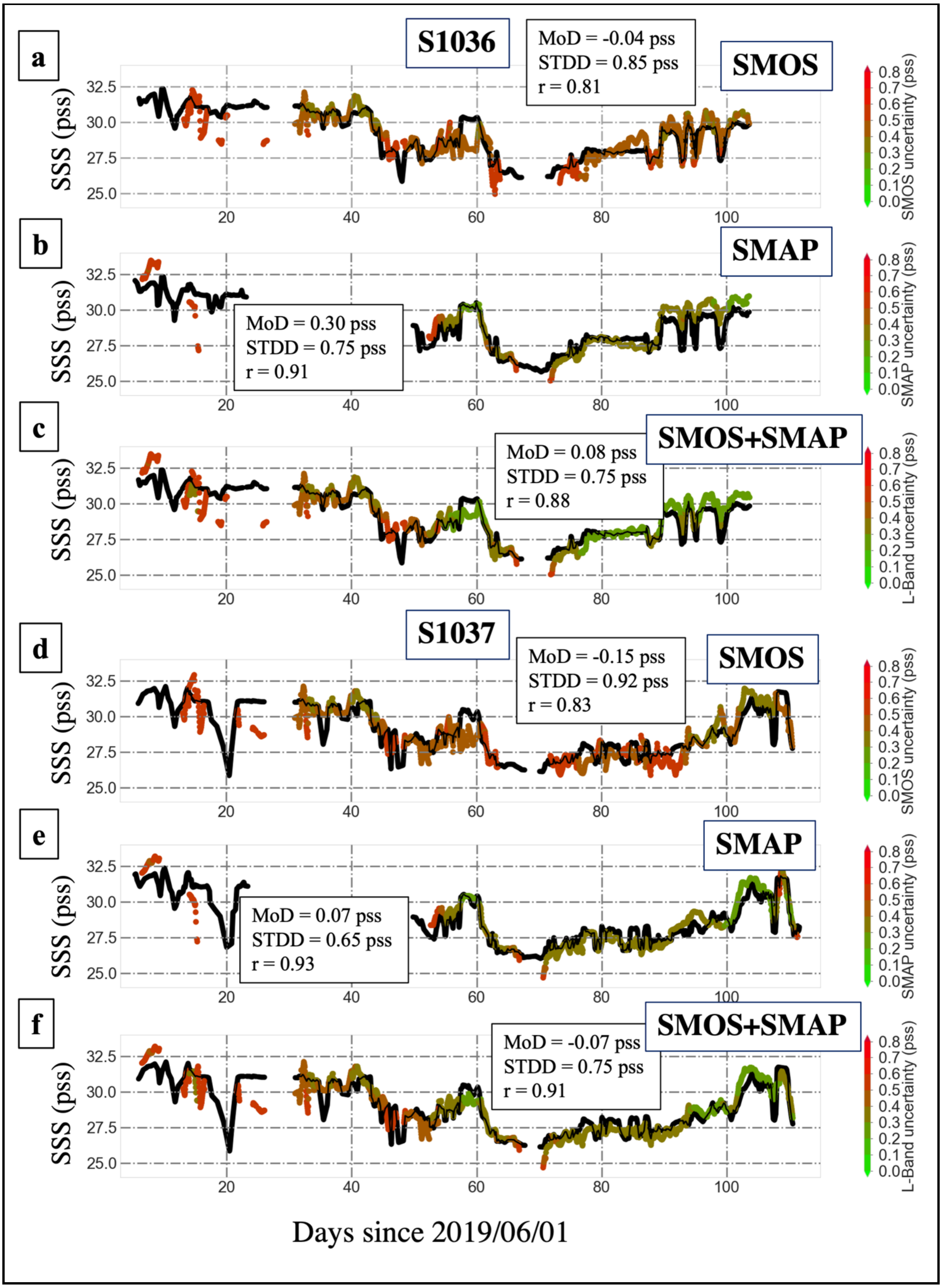

a
S1036
MoD = -0.04 pss
STDD = 0.85 pss
r = 0.81
SMOS
b
SMAP
MoD = 0.30 pss
STDD = 0.75 pss
r = 0.91
c
MoD = 0.08 pss
STDD = 0.75 pss
r = 0.88
SMOS+SMAP
d
S1037
MoD = -0.15 pss
STDD = 0.92 pss
r = 0.83
SMOS
e
SMAP
MoD = 0.07 pss
STDD = 0.65 pss
r = 0.93
f
MoD = -0.07 pss
STDD = 0.75 pss
r = 0.91
SMOS+SMAP
SSS (pss)
SMOS uncertainty (pss)
SMAP uncertainty (pss)
L-Band uncertainty (pss)
Days since 2019/06/01

Appendix-d: a) Saildrone 1036 SSS measurement (black) and SMOS collocated SSS in colour (colour for SSS uncertainty) timeseries; b) Saildrone 1036 SSS measurement (black) and SMAP collocated SSS in colour (colon for SSS uncertainty) timeseries; c) Saildrone 1036 SSS measurement (black) and L-Band collocated SSS in colour (colour for SSS uncertainty) timeseries; d) Saildrone 1037 SSS measurement (black) and SMOS collocated SSS in colour (colour for SSS uncertainty) timeseries; e) Saildrone 1037 SSS measurement (black) and SMAP collocated SSS in colour (colour for SSS uncertainty) timeseries; f) Saildrone 1037 SSS measurement (black) and L-Band collocated SSS in colour (colour for SSS uncertainty) timeseries.

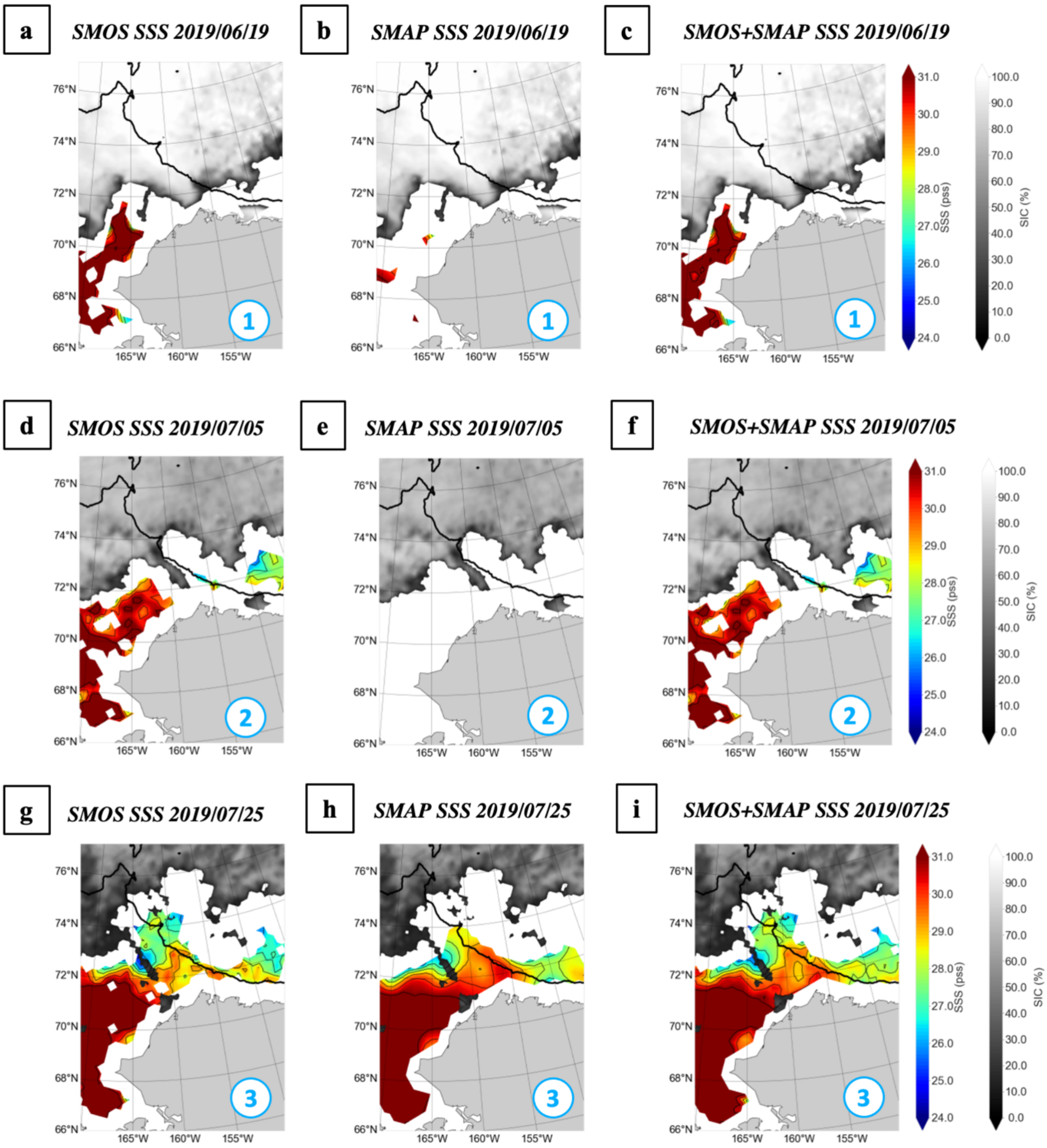

Appendix-e: a) SMOS SSS and OSI-SAF SIC for 2019/06/19; b) SMAP SSS and OSI-SAF SIC for 2019/06/19; c) L-Band SSS and OSI-SAF SIC for 2019/06/19; d) SMOS SSS and OSI-SAF SIC for 2019/07/05; e) SMAP SSS and OSI-SAF SIC for 2019/07/05; f) L-Band SSS and OSI-SAF SIC for 2019/07/05; g) SMOS SSS and OSI-SAF SIC for 2019/07/25; h) SMAP SSS and OSI-SAF SIC for 2019/07/25; i) L-Band SSS and OSI-SAF SIC for 2019/07/25.

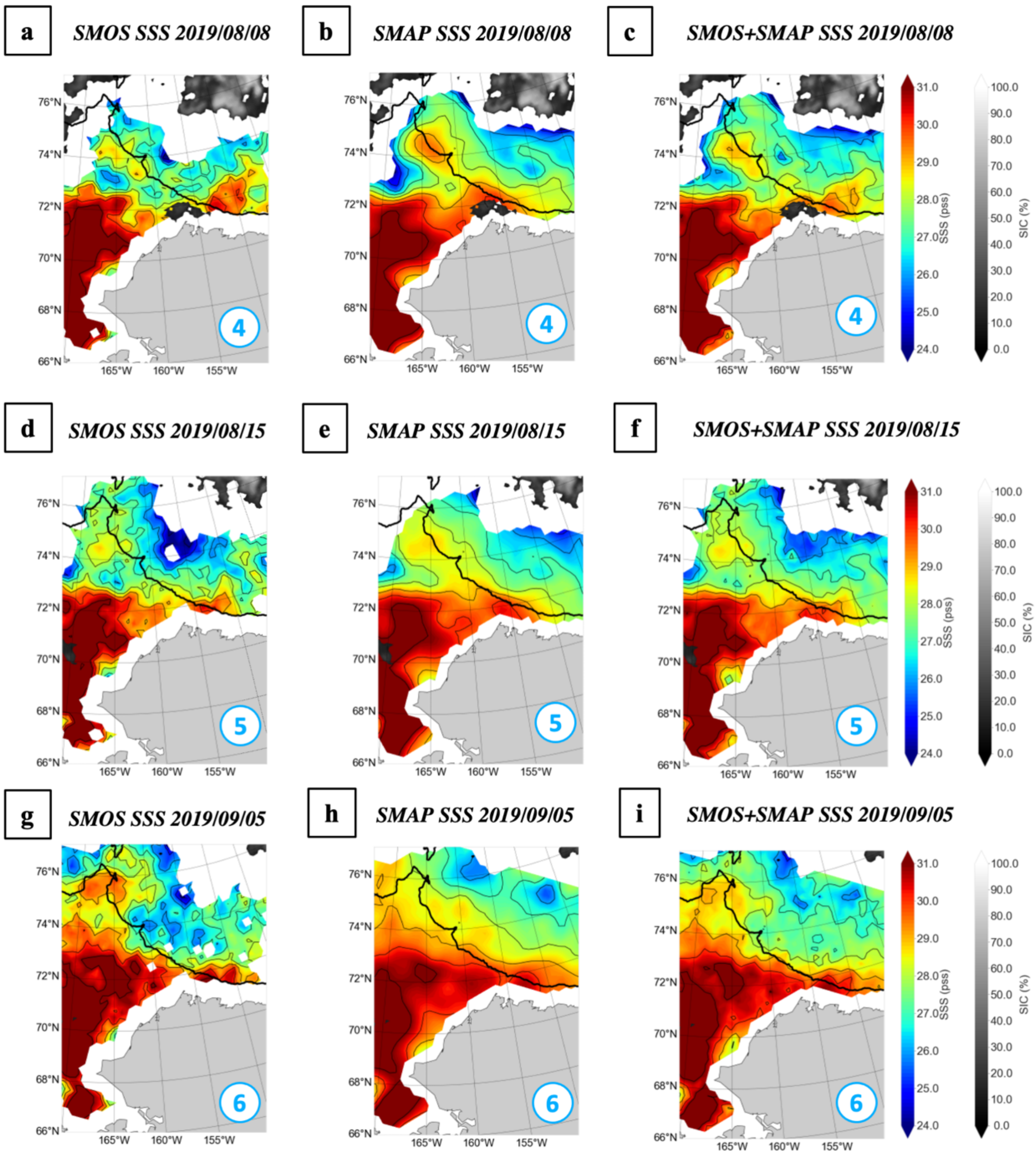

Appendix-f: a) SMOS SSS and OSI-SAF SIC for 2019/08/08; b) SMAP SSS and OSI-SAF SIC for 2019/08/08; d) L-Band SSS and OSI-SAF SIC for 2019/08/08; d) SMOS SSS and OSI-SAF SIC for 2019/08/15; e) SMAP SSS and OSI-SAF SIC for 2019/08/15; f) L-Band SSS and OSI-SAF SIC for 2019/08/15; g) SMOS SSS and OSI-SAF SIC for 2019/09/05; h) SMAP SSS and OSI-SAF SIC for 2019/09/05; i) L-Band SSS and OSI-SAF SIC for 2019/09/05.

Supporting information

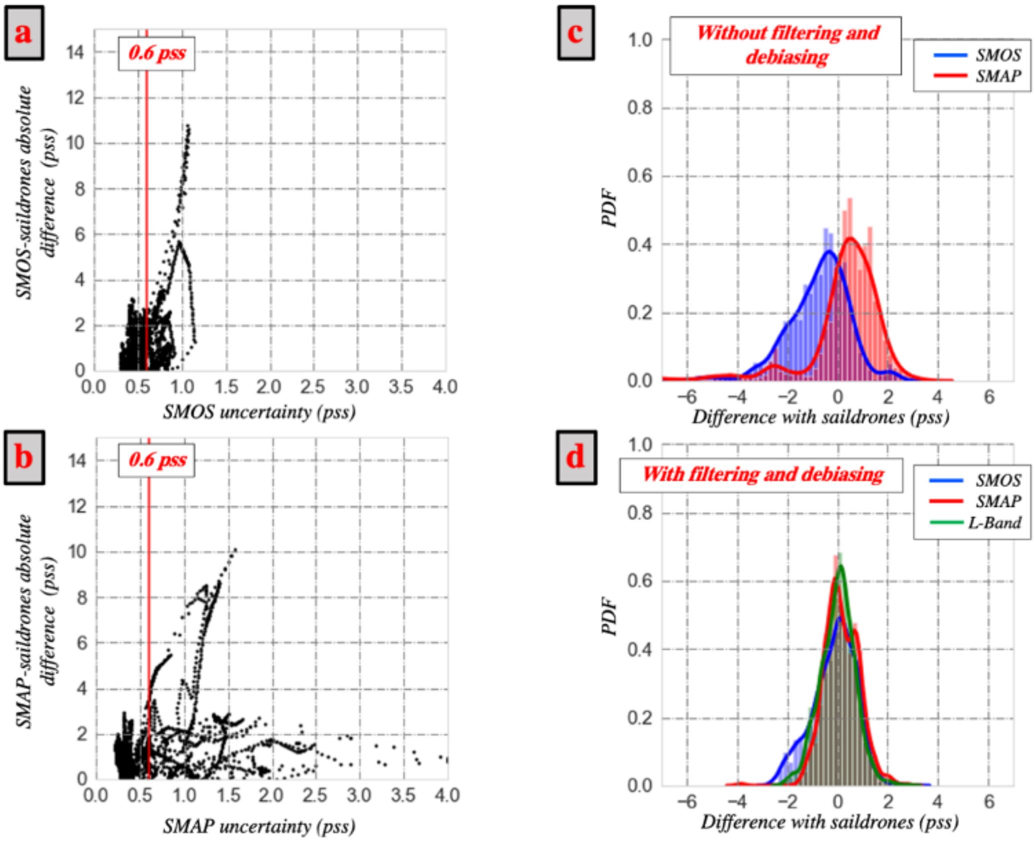

Appendix-a : A) Scatterplot of absolute difference between SMOS SSS and saildrones SSS versus SMOS SSS uncertainty (uncertainty threshold indicated in magenta); B) Scatterplot of absolute difference between SMAP SSS and saildrones SSS versus SMAP SSS uncertainty (uncertainty threshold indicated in magenta); C) Distributions of differences between SMOS and SMAP SSS, and saildrones SSS without filtering and debiasing; D) Distributions of differences between SMOS, SMAP and L-Band SSS, and saildrones SSS with filtering and debiasing.

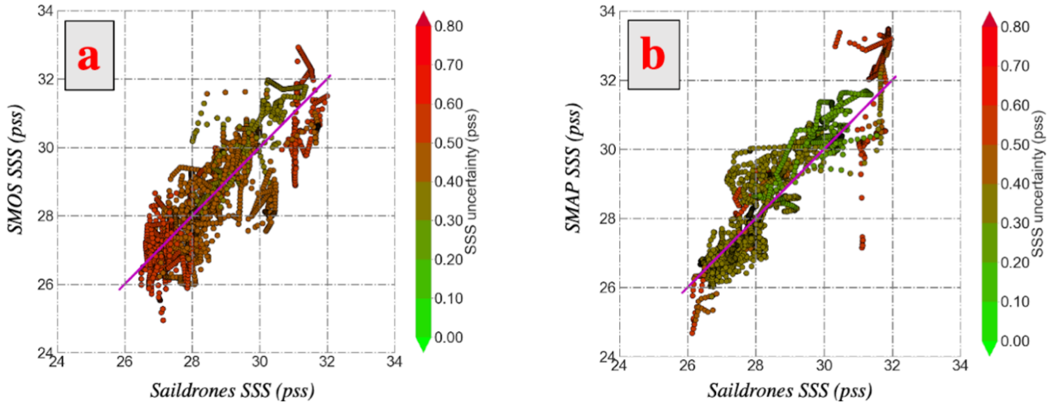

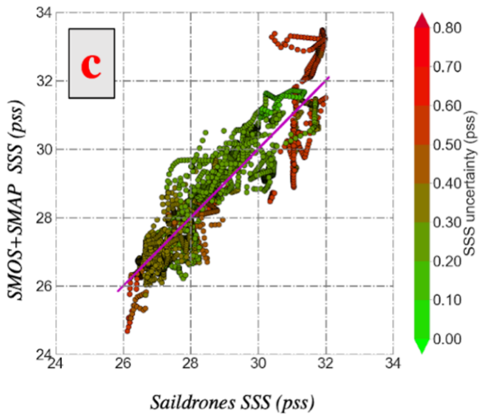

A) SMOS versus saildrones :
MoD = -0.12 pss
STDD = 0.88 pss
r = 0.81
N=2560

B) SMAP versus saildrones :
MoD = 0.17 pss
STDD = 0.71 pss
r = 0.92
N=2561

C) SMOS+SMAP versus saildrones :
MoD = 0.02 pss
STDD = 0.70 pss
r = 0.91
N= 2902

Appendix-b: Scatterplot of SSS, with satellite SSS retrieved uncertainties in colour: A) SMOS SSS versus Saildrones SSS; B) SMAP SSS versus Saildrones SSS; C) SMOS+SMAP SSS versus Saildrones SSS. Table is for statistical indicators (MoD = Mean of Difference, STDD = STandard Deviation of Difference, r = correlation coefficient and N = Number of collocations between satellite SSS and saildrone salinity).

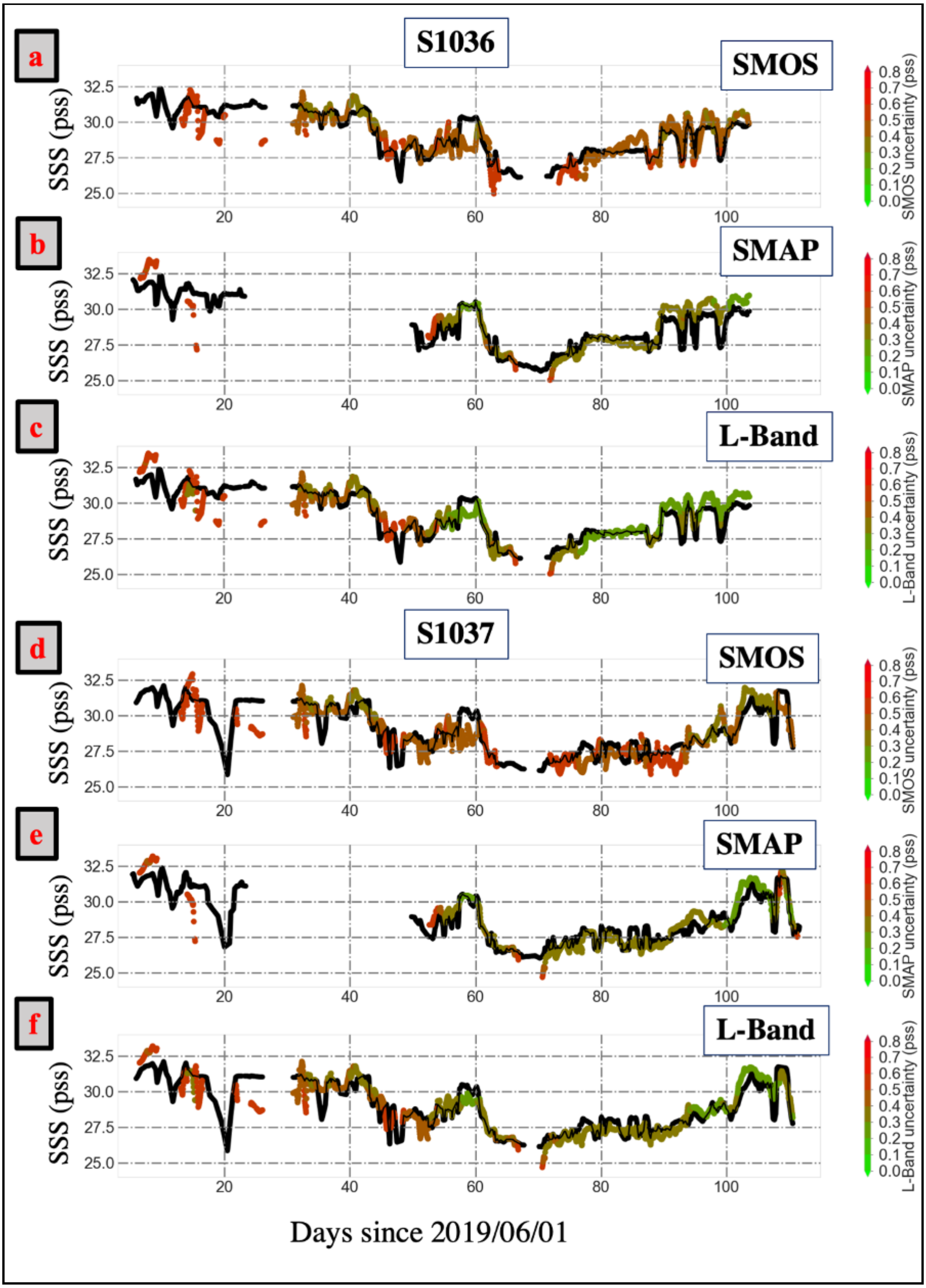
a
S1036
SMOS
SSS (pss)
SMOS uncertainty (pss)
b
SMAP
SSS (pss)
SMAP uncertainty (pss)
c
L-Band
SSS (pss)
L-Band uncertainty (pss)
d
S1037
SMOS
SSS (pss)
SMOS uncertainty (pss)
e
SMAP
SSS (pss)
SMAP uncertainty (pss)
f
L-Band
SSS (pss)
L-Band uncertainty (pss)
Days since 2019/06/01

Appendix-c : A) Saildrone 1036 SSS measurement (black) and SMOS collocated SSS in colour (colour for SSS uncertainty) timeseries; B) Saildrone 1036 SSS measurement (black) and SMAP collocated SSS in colour (colon for SSS uncertainty) timeseries; C) Saildrone 1036 SSS measurement (black) and L-Band collocated SSS in colour (colour for SSS uncertainty) timeseries; D) Saildrone 1037 SSS measurement (black) and SMOS collocated SSS in colour (colour for SSS uncertainty) timeseries; E) Saildrone 1037 SSS measurement (black) and SMAP collocated SSS in colour (colour for SSS uncertainty) timeseries; F) Saildrone 1037 SSS measurement (black) and L-Band collocated SSS in colour (colour for SSS uncertainty) timeseries.

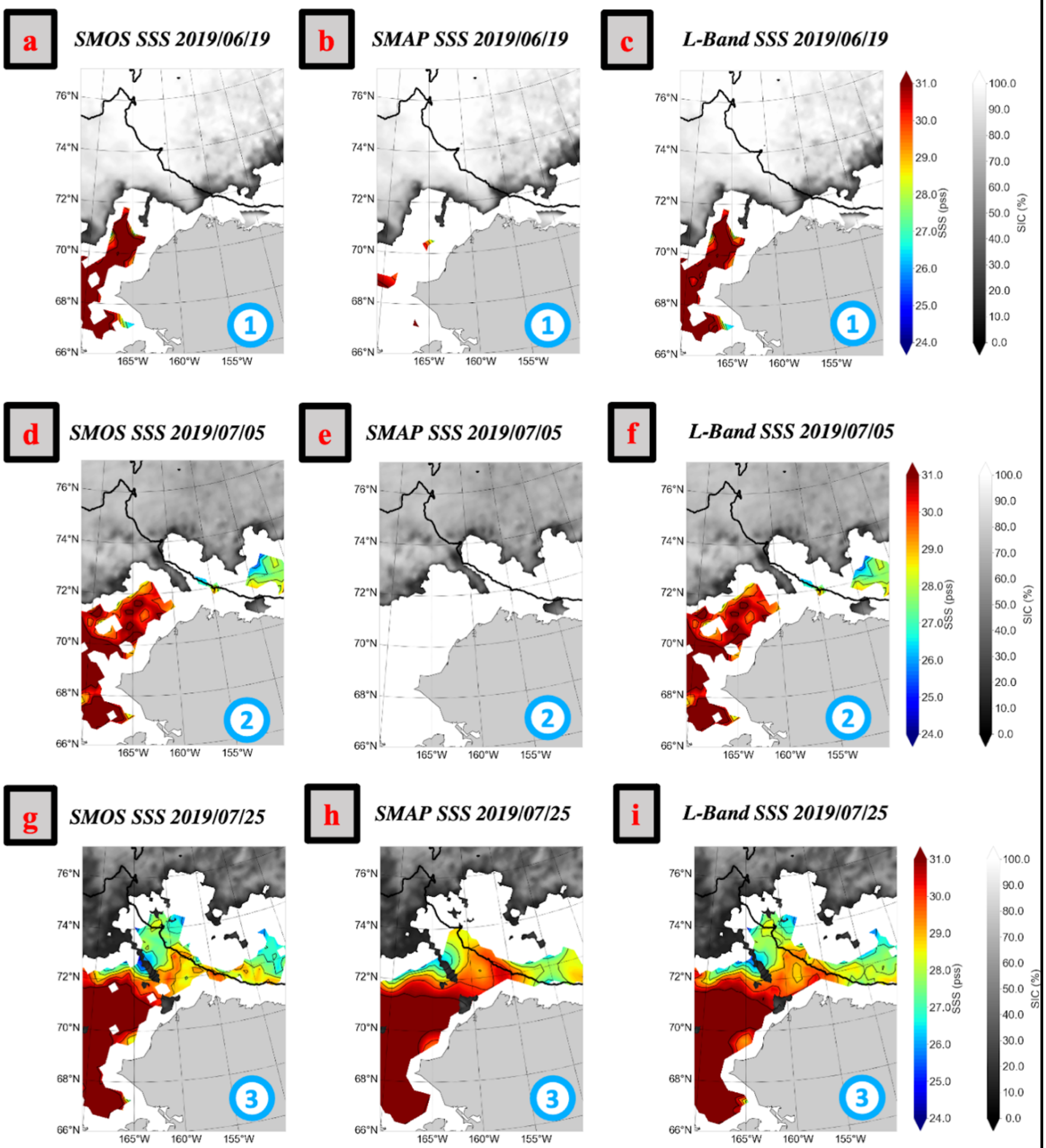

Appendix-d : A) SMOS SSS and OSI-SAF SIC for 2019/06/19; B) SMAP SSS and OSI-SAF SIC for 2019/06/19; C) L-Band SSS and OSI-SAF SIC for 2019/06/19; D) SMOS SSS and OSI-SAF SIC for 2019/07/05; E) SMAP SSS and OSI-SAF SIC for 2019/07/05; F) L-Band SSS and OSI-SAF SIC for 2019/07/05; G) SMOS SSS and OSI-SAF SIC for 2019/07/25; H) SMAP SSS and OSI-SAF SIC for 2019/07/25; I) L-Band SSS and OSI-SAF SIC for 2019/07/25.

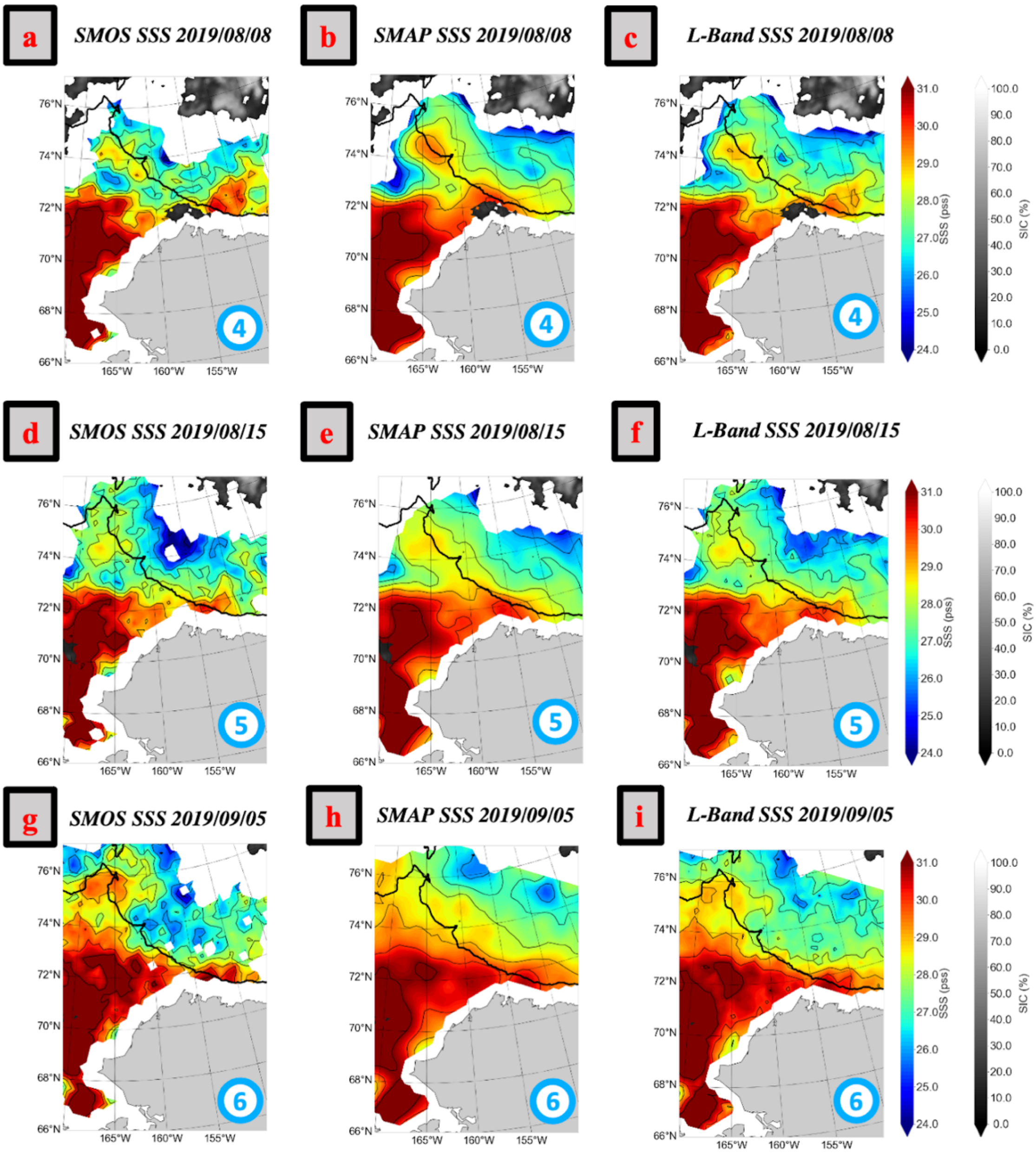

Appendix-e : A) SMOS SSS and OSI-SAF SIC for 2019/08/08; B) SMAP SSS and OSI-SAF SIC for 2019/08/08; C) L-Band SSS and OSI-SAF SIC for 2019/08/08; D) SMOS SSS and OSI-SAF SIC for 2019/08/15; E) SMAP SSS and OSI-SAF SIC for 2019/08/15; F) L-Band SSS and OSI-SAF SIC for 2019/08/15; G) SMOS SSS and OSI-SAF SIC for 2019/09/05; H) SMAP SSS and OSI-SAF SIC for 2019/09/05; I) L-Band SSS and OSI-SAF SIC for 2019/09/05.